Primary Somatosensory Cortex Bidirectionally Modulates Sensory Gain and Nociceptive Behavior in a Layer-Specific Manner

Katharina Ziegler[1*], Jan Burghardt[1*], Ross Folkard[1*], Antonio J Gonzalez[1*], Sailaja Antharvedi-Goda[1], Jesus Martin-Cortecero[1], Emilio Isaías-Camacho[1], Sanjeev Kaushalya[2], Linette Liqi Tan[3], Thomas Kuner[4], Rohini Kuner[3], Rebecca Mease[1#] and Alexander Groh[1#]

1 Medical Biophysics, Institute for Physiology and Pathophysiology, Heidelberg University, Germany
2 Cold Spring Harbor Laboratory, Cold Spring Harbor, New York, USA
3 Institute for Pharmacology, Heidelberg University, Germany
4 Institute for Anatomy, Heidelberg University, Germany
* Equal first authors, # equal last authors

Abstract

The primary somatosensory cortex (S1) is the hub for body sensation of both innocuous and noxious signals, yet its role in somatosensation versus pain is debated. Despite known contributions of S1 to sensory gain modulation, its causal involvement in subjective sensory experiences remains elusive. Unspecific bulk manipulations of S1 activity have not disambiguated the precise role of the S1 in nociception and pain. Here, using cell-type-specific manipulations in mouse S1 we reveal the involvement of two major cortical output neuron types in layers 5 (L5) and 6 (L6) in the perception of innocuous and noxious somatosensory signals. We find that L6 neurons can drive aversive hypersensitivity and spontaneous nocifensive behavior. L6 downstream effects revealed enhanced thalamic somatosensory responses, and in parallel, strong suppression of L5 neurons, pointing towards an anti-nociceptive function of L5 output. Indeed, targeted L5 activation reduced sensory sensitivity and normalized inflammatory allodynia, thus revealing a layer-specific and bidirectional role for S1 in modulating subjective sensory experiences.

Introduction

Flexible modulation of sensory gain is a canonical thalamocortical circuit function, serving to sharpen sensory information streams *en route* to the cortex [1–3] and thereby adaptively drive perception and behavior [4]. Advances in recording technology and cell-type-specific interventions have allowed delineation of cell-type-specific contributions to gain control, particularly between specific cortical output pathways from pyramidal tract (PT) neurons in layer 5 (L5), which target diverse subcortical structures, and corticothalamic (CT) neurons in layer 6 (L6) [5,6]. The emerging consensus is that L6-CT neurons of primary sensory cortices control cortical gain by simultaneously recruiting cortical inhibitory neurons [7–9] and modulating multiple cellular and circuit mechanisms in the thalamus [1,10–14].

As a consequence, L6-CT pathways support flexible detection of behaviorally relevant signals by dynamically sculpting both thalamic input to cortex and cortical sensitivity to thalamic inputs. These L6 functions have been evaluated from the standpoint of gain control as beneficial to sensory processing, attention, and perception. However, such tuning of sensitivity could potentially give rise to maladaptive mismatch between cortical gain and the sensory environment, for example promoting hypersensitivity. As the L6-CT function appears conserved across thalamocortical systems for most sensory modalities, imbalances in these circuits could contribute to functionally adverse outcomes in sensory processing. This potential “dark side” of CT gain modulation is particularly pertinent for circuits involved in pain, as these circuits link sensory and affective functions to generate both healthy and pathological pain perceptions [15–17].

Primary somatosensory cortex S1 receives both innocuous and noxious signals via thalamocortical (TC) inputs from ventral posterolateral (VPL) thalamus, and is therefore a primary junction at which normal body sensations could be amplified into pain or, conversely, painful signals could be suppressed [16,18]. In turn, S1’s output is broadcast to thalamic nuclei via the L6-CT pathway and to several subcortical targets via the PT pathway [5,6]. Thus, S1 could potentially modulate ascending pain signals at various subcortical points, including VPL, which is tightly linked to different pain states [19–25].

Indeed, tantalizing yet heterogenous reports that broad manipulations of S1 alter affective pain responses [26,27] and the discovery of a causal link between S1 gamma-activity and pain [28,29] have challenged the view that S1 generates strictly sensory-discriminative aspects of pain

[15,30–33]. However, the prevalent use of bulk manipulations and lesions of S1 [34,35] has led to controversial views on whether S1 is at all involved in affective pain processes [36,37]. Moreover, while significant evidence exists for CT and PT involvement in healthy sensory processing and cognition, only sparse evidence involves S1 output pathways in pain and pathology [38]. In particular, while PT neurons have been linked to neuropathic pain [26,39] and nociceptive signaling in spinal circuits [40], the involvement of L6-CT pathways in pain has received limited attention [30,41], despite an established role for sensory gain control in all sensory modalities studied to date.

We hypothesized a link between S1-CT gain modulation and the subjective dimensions of sensory experiences, which may contribute to the generation of painful sensations. To test this hypothesis, we probed how L6-CT projections from S1 modulate sensitivity to innocuous and noxious stimuli in mice, using behavioral read-outs, targeted optogenetics, and high-yield electrophysiology in the VPL-S1 TC system.

We report that L6-CT – but not L5-PT – activation triggers hypersensitivity and aversion in behaving mice, suggesting that L6-CT gain amplification can contribute to functionally adverse outcomes in sensory processing. Probing the neural basis of this effect with *in vivo* electrophysiology demonstrated that L6 activation enhances TC signaling at the level of VPL and superficial layers of S1. In parallel, L6 stimulation largely silenced L5 neurons, suggesting that the pronociceptive effect of L6 may result from both enhancement of primary sensory signaling circuits and simultaneous dampening of the wide-reaching L5-PT system. In turn, L5 activation had an antinociceptive effect, decreasing mechanical sensitivity and normalizing inflammatory allodynia. Together, these findings reveal bidirectional control over somatosensation by discrete S1 corticofugal circuits, suggesting future avenues for treating pain-related and sensory processing disorders.

Results

The Ntsr1-Cre mouse line is a useful model to study L6-CT pathways in different sensory cortices, including S1 cortex [6–8,10,13,14,42]. To assess the role of L6-CT neurons in modulating sensory gain and nociception, we targeted channelrhodopsin-2-EYFP (ChR2) or EGFP expression to L6 of the right S1 hindlimb cortex (S1HL) of Ntsr1-Cre mice via stereotaxic injections of AAV-DIO-ChR2-EYFP ("L6-ChR2 mice") or AAV-DIO-EGFP ("L6-EGFP mice"). Transgene expression in L6-ChR2 and L6-EGFP mice was restricted to L6 neurons in S1HL

and their corticothalamic axons (Fig. 1a; L6-EGFP Supplementary Fig. 1b). Silicon probe recordings in anesthetized L6-ChR2 mice validated optogenetic activation of L6-CT neurons in S1HL, demonstrating robust optogenetic drive of short-latency, temporally precise L6 spiking (Fig. 1b) that persisted throughout the 5 second laser stimulus (Fig. 1c).

Optogenetically-evoked L6-CT activity in the S1HL cortex elicits spontaneous nocifensive behavior.

We asked whether L6-CT activation in the S1HL cortex has any measurable effect on spontaneous behavior in the absence of peripheral sensory stimulation (Fig.1e). We found that in awake, freely moving animals implanted with a fiber optic above S1HL, optogenetic activation of L6-CT neurons elicited vigorous lifting and shaking of the contralateral hindlimb in a laser intensity-dependent manner (Fig. 1f). Laser stimulation at the maximal intensity (318.18 mW/mm^2 at the fiber tip, 1.54 mW/mm^2 at the level of L6, see Methods) evoked paw lifting and limb shaking in a majority of animals (9/11 and 6/11, respectively; Supplementary video 1) and vocalizations (not shown). At this intensity, these expressions of nocifensive behavior [43] were robustly evoked in the majority of stimulation trials (paw lifting in 86% of trials; limb shaking in 73% of trials) and were absent in the EGFP-expressing control animals. The manifestation of these vigorous responses, specifically to the contralateral hindlimb, suggests that L6-CT activation in HL cortex can evoke a nociceptive experience originating from the hindlimb, even in the absence of peripheral sensory stimulation.

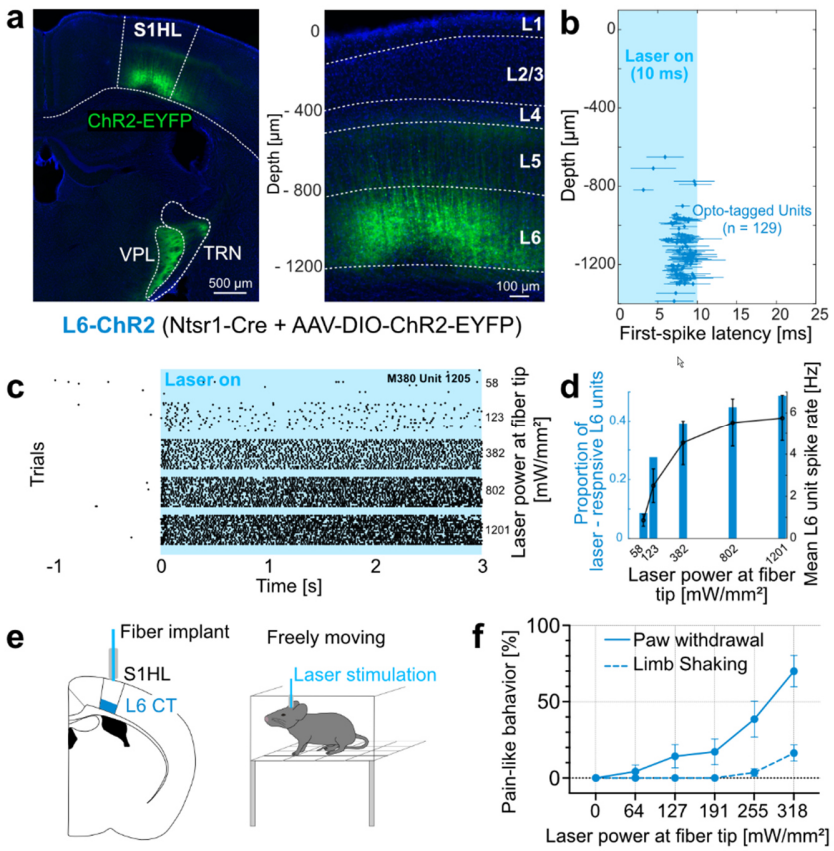

Fig. 1: L6-CT activation in the S1HL cortex elicits nocifensive behaviors in the absence of peripheral stimulation.

(a) Expression of ChR2-EYFP (green) in S1HL of a L6-ChR2 mouse showing fluorescence in L6-CT neurons and their axons in the VPL and thalamic reticular nucleus (TRN). Magnification of S1HL cortex (right panel) with L6-CT neurons depth-registered relative to S1HL layer borders (dashed lines, estimated based on soma sizes and densities using DAPI signals, blue).

(b-d) S1HL cortex silicon probe recording from L6-ChR2 mice demonstrating graded optogenetic control of the L6-CT units. **(b)** L6-CT units were identified based on their short-latency, low jitter response to 10 ms light pulses. Each marker shows unit depth vs. mean ± SD latency to first evoked spike (pooled from 3 animals, laser strength: 1201 mW/mm²). **(c)** Example rasters for a laser-responsive L6-CT unit (depth = 1205 µm). **(d)** Blue bars: fraction of laser-responsive L6 units (from n = 232 L6 units total) as a function of laser power. Black: corresponding mean spiking rate (mean ± SEM, n = 92 units; mean depth ± SD = 1194 ± 141 microns). Data from a representative experiment (n = 3 mice).

(e) Schematic of fiber optic implant for optogenetic L6-CT stimulation in freely moving mice.

(f) Quantification of pain-like behaviors, paw lifting (blue solid line) and limb shaking (blue dashed line), elicited by optogenetic activation of S1HL L6-CT neurons in the absence of sensory stimulation (n = 11 mice). See also Supplementary Video 1.

Optogenetically-evoked L6-CT activity in the S1HL cortex induces hypersensitivity, exacerbates inflammatory allodynia and induces aversion.

The ability of L6-CT neurons to elicit spontaneous nocifensive behavior (Fig. 1e) suggests that this pathway's activity is sufficient to induce a state of hypersensitivity and, contrary to a strict sensory discriminatory role, implicates S1 in regulating emotional-affective aspect of pain. We tested these hypotheses by assessing mechanical and noxious heat sensitivity as a function of L6-CT activation and by quantifying aversive effects of L6-CT activation in a conditioned place preference paradigm.

To quantify mechanical sensitivity we used the Von Frey test [44,45] to measure hindpaw withdrawal probabilities in response to mechanical stimulation over a range of stimulation forces (0.04 g - 2 g), with and without optogenetic stimulation of L6-CT neurons in the contralateral S1HL (Fig. 2a, b). Using optogenetic laser intensities below the spontaneous paw lifting threshold (see Methods), L6-CT activation increased mechanical sensitivity over nearly the entire range of tested mechanical forces ($p < 0.001$). Increased sensitivity to low pressure punctate stimuli (0.04 - 0.4 g) [46] suggests an allodynic effect of L6-CT activity in S1 (i.e. a nociceptive response to typically innocuous stimuli), while increased sensitivity to nociceptor-activating mechanical forces (0.6 - 2 g) [47] represents a hyperalgesic effect. Mechanical sensitivity remained unchanged in control animals (Ntsr1-Cre mice expressing EGFP in L6-CT; Supplementary Fig. 2b).

These nociceptive hypersensitivity-inducing functions of L6-CT neurons in healthy animals prompted us to ask if and how this pathway interacts with a preexisting pain condition. We therefore repeated von Frey experiments in an inflammatory pain model induced by injection of Complete Freund's adjuvant (CFA) in the left hindpaw, which led to mechanical hypersensitivity to innocuous and noxious stimuli (Supplementary Fig. 3), as shown before [29]. L6-CT activation in contralateral S1HL further increased mechanical sensitivity (Fig. 2c) in contrast to L6-EGFP controls in which sensitivity remained unchanged (Supplementary Fig. 2j). To better compare the L6-CT effects on mechanical sensitivity in naive and CFA-treated mice, we computed filament force thresholds that elicited paw withdrawal in 60% of trials, as a measure of overall sensitivity (Fig. 2d). Taken together, L6-CT activation induced mechanical hyperalgesia and allodynia in naive animals, and exacerbated these effects in an inflammatory model.

While response to von Frey filaments is an established measure of testing mechanical sensitivity in response to innocuous and noxious stimuli, we sought to validate the pronociceptive functions of the L6-CT pathway with a purely noxious stimulus. We therefore used the Hargreaves test, an established measure of heat-induced nociception[48] to assess if L6-CT activity can modulate responses to pain-inducing heat stimulation. L6-CT stimulation significantly reduced paw withdrawal latencies in response to infrared heat stimulation of the hindpaw by ~30%, demonstrating a causal link between L6-CT activity and increased heat sensitivity (Fig. 2f). Heat sensitivity remained unchanged in L6-EGFP control animals.

Because L6-CT activation can elicit a seemingly distressful and aversive experience (Fig. 1, Supplementary video 1) we sought to directly test the link between L6-CT activity in S1HL and negative affect by employing a real-time aversion paradigm [29]. Here, mice (L6-ChR2 and L6-EGFP controls) freely roamed a two-chamber setup during five baseline sessions to establish individual chamber preferences. In subsequent conditioning sessions, preferred chambers were paired with laser stimulation of the right S1HL cortex (schematic in Fig. 2g). Changes in the time spent in the preferred chamber were used to quantify aversive effects of the stimulation.

L6-ChR2 but not L6-EGFP control mice spent significantly less time in the chamber paired with optogenetic stimulation relative to the time spent in the same chamber during the baseline session (i.e. without optogenetic stimulation) (Fig. 2h, i). While chamber preference indices (ΔPIs) show that optogenetic laser stimulation decreased the preference for the paired chamber in both L6-ChR2 and L6-EGFP mice, the effect was significantly stronger in L6-ChR2 mice, for which L6-CT stimulation caused complete preference for the unpaired chamber (Fig. 2j). The reduced preference index in L6-EGFP mice may indicate that the laser itself is optically aversive, independent of L6-CT engagement. In summary, optogenetically-evoked L6-CT activity in the S1HL cortex elicits aversive avoidance in mice.

In conclusion, these experiments not only demonstrate that L6-CT neurons in S1HL cortex can increase paw sensitivity, but also reveal that such gain enhancement can lead to negative affective consequences, including amplified nociception and aversion.

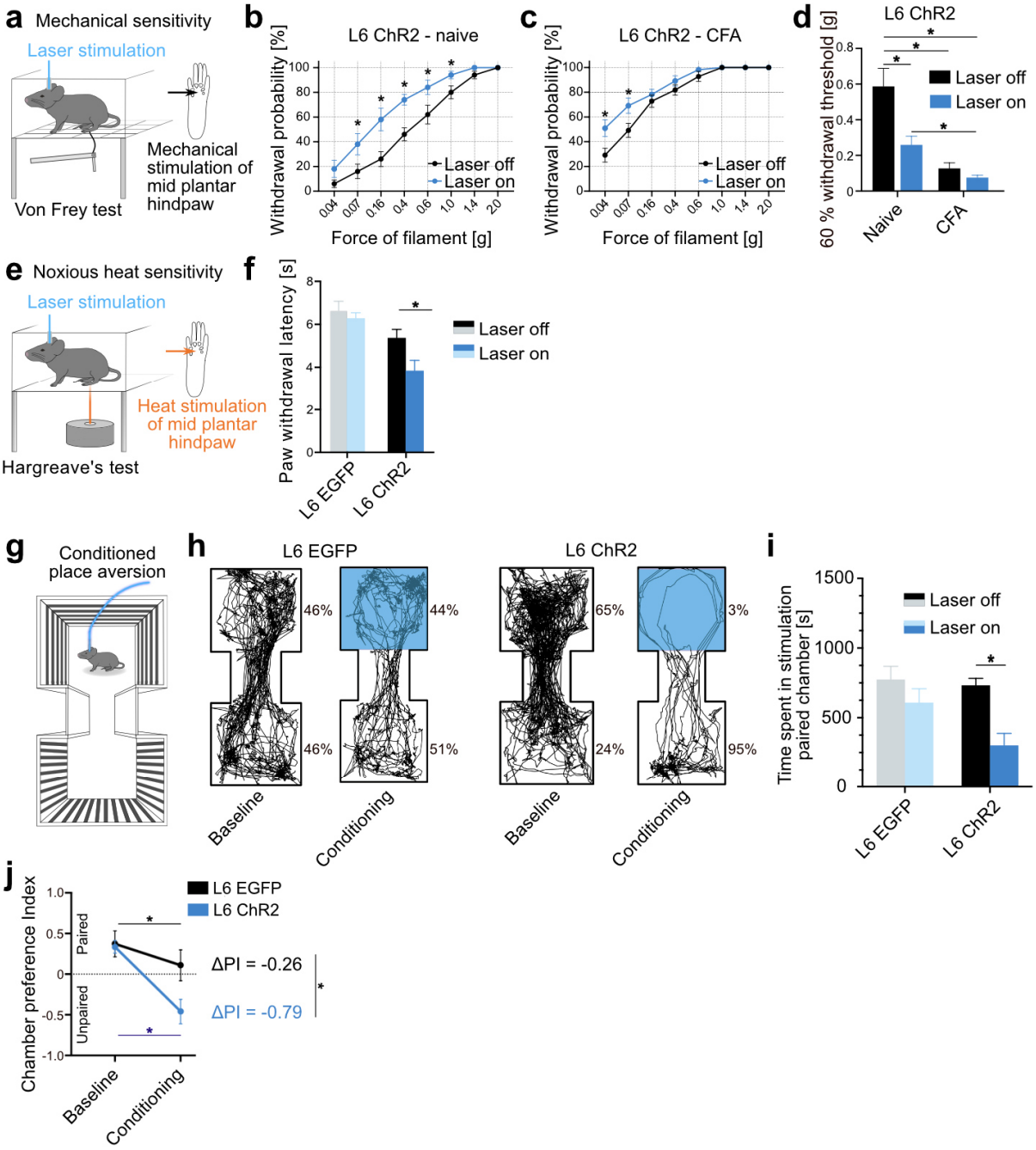

Fig. 2: L6-CT activation in the S1HL cortex increases mechanical and thermal sensitivity, exacerbates inflammatory allodynia, and induces aversion.

(a) Schematic of Von Frey setup to quantify mechanical sensitivity in response to graded force stimulation of the hindpaw with and without optogenetic stimulation of L6-CT in S1HL.

(b) Within-animal comparison of paw withdrawal probabilities in response to graded von Frey stimulation of the left hindpaw with (blue, Laser on, 5 s continuous pulse) and without (black,

Laser off) L6-CT stimulation in S1HL (n = 10 mice). L6-EGFP control animals in Supplementary Fig. 2b.

(c) Same as in **(b)** but after animals were injected with Complete Freund's adjuvant (CFA) in the left hindpaw to induce paw inflammation (n = 10 mice). For the comparison of pre- and post-CFA withdrawal probabilities see Supplementary Fig. 3.

(d) Comparison of filament forces that evoked paw withdrawal in 60% of the stimulation trials as a function of L6-CT activation without (Naive) and with (CFA) inflammation (n = 10 mice). Lower filament forces indicate increased sensitivity.

(e) Schematic of Hargreaves setup to quantify noxious heat sensitivity in response to noxious heat laser stimulation (orange) of the hindpaw with and without optogenetic stimulation of L6-CT in S1HL.

(f) Paw withdrawal latencies in response to heat stimulation of the left hindpaw with (blue, Laser on, 5 s continuous pulse) and without (black/gray, Laser off) optogenetic stimulation of L6-CT in S1HL of L6-EGFP (n = 5) and L6-ChR2 (n = 7) mice.

(g) Schematic of experimental setup to measure real-time place aversion as a function of optogenetic stimulation of L6-CT in the S1HL.

(h) Example animal tracking plots from L6-EGFP and L6-ChR2 mice, recorded at baseline and during conditioning with 20 Hz laser stimulation of the S1HL cortex; area highlighted in blue indicates the laser-paired chamber; mice received no stimulation in the other chamber. Percentages show relative time spent in each chamber.

(i) Population analysis of total time spent in the laser-paired chamber at baseline (Laser off, black/gray) and during stimulation (Laser on, blue, 20 Hz laser stimulation in S1HL cortex) of L6-EGFP (n = 5) and L6-ChR2 (n = 7) mice.

(j) Average chamber preference indices (PI) for L6-ChR2 (n = 7 mice) and L6-EGFP (n = 5 mice), computed for the last baseline session and the first stimulation session. A PI of 1 indicates a full preference for the paired chamber, while a PI of -1 indicates a full preference for the unpaired chamber, i.e. full avoidance of the laser-paired chamber.

* represents $p < 0.05$; 2b-j: Repeated measures ANOVA with post-hoc Bonferroni test, j: L6 CPA change in preference indices, one-tailed unpaired t-Test test. Exact F and p values in Suppl. Table 1. Data are shown as mean ± S.E.M.

Dissecting the neuronal circuit mechanisms underlying the pronociceptive effect of L6-CT activation.

We hypothesized that the pronociceptive effect of L6-CT stimulation during behavior arises from enhancement of sensory signaling in the thalamus, in light of the established role for L6-CT modulation of thalamic nuclei in other modalities [1,10,14]. In addition, the effect of L6 might also involve cortico-cortical components, given that L6-CT neurons recruit local and translaminar cortical inhibitory neurons [8,9,42]. To identify possible cell-type-specific corticothalamic and cortico-cortical contributions to the observed spontaneous (Fig. 1) and stimulus-evoked (Fig. 2) pain-related behaviors, we recorded VPL (Fig. 3) and translaminar

S1 single unit spiking (Fig. 4) with silicon probes (Fig. 3a schematic, Supplementary Fig. 4) in combination with optogenetics and plantar mechanical stimulation in anesthetized Ntsr1-Cre mice expressing ChR2 in L6-CT neurons in S1HL cortex.

We assessed single-unit VPL (Fig. 3) and S1 (Fig. 4) spiking in three stimulation conditions (Fig. 3a): 1) Laser (L) stimulation of L6-CT neurons, 2) Mechanical (M) stimulation of the hindpaw, and 3) combined mechanical and laser (ML) stimulation. To ameliorate the effects of initial peak synchrony in the L6-CT population, in the ML condition, the laser onset preceded the mechanical stimulus by approximately 0.5 s (Figs. 3a, 4a). After pooling recordings across animals, we first screened for units with spiking responses significantly modulated relative to baseline in any of the three stimulus conditions (see Methods). The majority of units met this criterion (742/1018 in VPL, 751/842 in S1HL) and the remainder were not analyzed further. The response of each unit was further quantified as mean firing rate ($\bar{r}$) measured in a 1.5 s window after stimulus onset and modulation index (MI, -1 to 1) calculated by comparing stimulus-evoked spiking to baseline spiking. For VPL units, we also calculated burst probability (BP, 0-1), the ratio of burst events out of all observed responses, and response probability (RP, 0-1) per stimulus presentation.

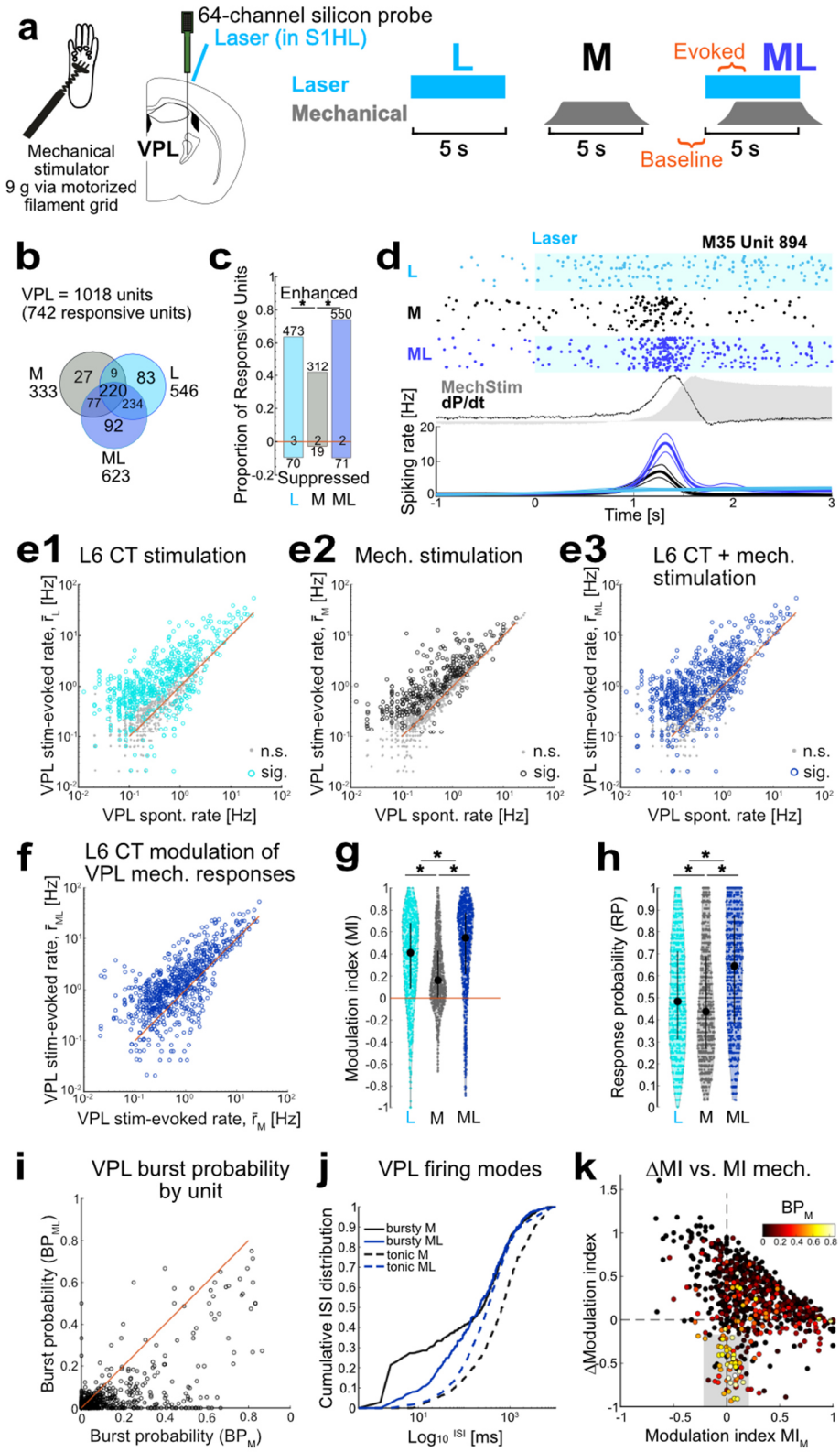
a
64-channel silicon probe
Laser (in S1HL)
Mechanical stimulator
9 g via motorized filament grid
VPL
Laser
Mechanical
L
M
Evoked
ML
5 s
5 s
Baseline
5 s
b
VPL = 1018 units
(742 responsive units)
M 333
L 546
ML 623
27
9
83
220
77
234
92
c
Proportion of Responsive Units
Enhanced
473
312
550
Suppressed
70
19
71
L M ML
d
Laser
M35 Unit 894
L
M
ML
MechStim
dP/dt
Spiking rate [Hz]
Time [s]
e1 L6 CT stimulation
e2 Mech. stimulation
e3 L6 CT + mech. stimulation
VPL stim-evoked rate, $\bar{r}_L$ [Hz]
VPL stim-evoked rate, $\bar{r}_M$ [Hz]
VPL stim-evoked rate, $\bar{r}_{ML}$ [Hz]
VPL spont. rate [Hz]
n.s.
sig.
f L6 CT modulation of VPL mech. responses
VPL stim-evoked rate, $\bar{r}_M$ [Hz]
g
Modulation index (MI)
L M ML
h
Response probability (RP)
i VPL burst probability by unit
Burst probability (BP_{ML})
Burst probability (BP_M)
j VPL firing modes
bursty M
bursty ML
tonic M
tonic ML
Cumulative ISI distribution
Log10 ISI [ms]
k ΔMI vs. MI mech.
BP_M
ΔModulation index
Modulation index MI_M

Fig. 3: L6-CT activation enhances VPL output to cortex.

(a) Left: Schematic of VPL silicon-probe recordings in anesthetized mice (n = 4). Right: stimulation protocol for three interleaved stimulation conditions: L6-CT activation (L), mechanical paw stimulation (M), and combined L6-CT + mechanical simulation (ML). Windows for unit spike analysis indicated in orange.

(b) Population overlap in L/M/ML conditions. 742/1018 VPL units were significantly modulated in at least one stimulus condition; 92 units were only responsive to ML.

(c) Proportion and counts of enhanced and suppressed VPL units for each L/M/ML condition. For example, ~40% of the VPL units were enhanced by mechanical stimulation (M), while during the ML condition 75% were enhanced and ~10% were suppressed. A minority of units had only changes in spike timing, not spike counts (counts at zero).

(d) Example VPL single unit responses to L, M, and ML stimulation. Top: raster examples; middle: mechanical pressure (gray shading) and first temporal derivative of pressure (dP/dt, black); bottom: corresponding PSTHs (bin size = 20 ms, smoothed with BARS method [49]).

(e1,2,3) Stimulus-evoked spiking rate ($\bar{r}_L$, $\bar{r}_M$, $\bar{r}_{ML}$) vs. spontaneous spiking rate by unit. Open markers: significantly modulated units in each condition (n = 536, 333, 623, for L, M, ML, respectively). Filled circles: not significantly modulated. Diagonal lines indicate equal responses. Central tendency and dispersion presented as (1st quartile **median** 3rd quartile): $\bar{r}_L$ (0.54 **1.07** 2.60) Hz, $\bar{r}_M$ (0.47 **0.99** 2.3) Hz, $\bar{r}_{ML}$ (0.69 **1.31** 3.24) Hz.

(f-h) ML condition enhances VPL responses. **(f)** Comparison of $\bar{r}_{ML}$ vs. $\bar{r}_M$ (0.54 **1.14** 2.81) Hz and (0.27 **0.67** 1.71) Hz, respectively, for all VPL units showing modulation in any condition (n = 742). L6-CT-evoked difference in spiking rate ($\Delta\bar{r} = \bar{r}ML-\bar{r}_M$): (0.02 **0.45** 1.19).

Both **(g)** stimulus-evoked modulation index (MI) and **(h)** response probability (RP) per trial varied by condition and were greatest in the ML condition. Black markers and bars show median and IQR. **(g)** MI_L (0.09 **0.41** 0.68), MI_M (0.00 **0.16** 0.43) and MI_{ML} (0.22 **0.55** 0.77) and **(h)** RP_L (0.31 **0.48** 0.71), RP_M (0.27 **0.44** 0.69) and RP_{ML} (0.39 **0.65** 0.87). $MI_{ML} > MI_L > MI_M$ and $RP_{ML} > RP_L > RP_M$.

(i) L6-CT activation decreases VPL burst probability (BP). BP = 0 and BP = 1 indicate all tonic or burst spiking, respectively, while BP = 0.1 indicates 10% of spiking events were bursts with 2 or more spikes. Scatter plot: BP of stimulus-evoked spiking, BP_{ML} vs. BP_M, for each unit shown in **g** (638/742 units significantly different). BP_{ML} (0 **0.016** 0.047) < BP_M (0 **0.032** 0.144).

(j) L6-CT activation regularizes stimulus-evoked spike timing in VPL. Cumulative interspike interval (ISI) distributions for M and ML conditions for bursty (BP > 0.1, solid line, n = 227) and tonic (BP ≤ 0.1, dashed, n = 515) units. Data shown as the median per 1 ms bin for ISI distributions calculated separately for each unit.

(K) Scatter plot: ΔMI vs. MI_M for individual units ($\Delta MI = MI_{ML} - MI_M$). Each unit is colored by BP_M. A subset of bursty units had near-zero MI_M and $MI_{ML} < 0$ (gray box), suggesting that non-sensory coding VPL units are suppressed by L6-CT activation which further increases the overall proportion of sensory-driven VPL spike output.

* represents $p < 0.05$; 3c: Chi-squared test followed by Marascuillo procedure, e,f: Wilcoxon signed-rank or ZETA test, g,h: Friedman test with post-hoc Wilcoxon signed-rank test, i: delta BP, McNemar's test; BP_{ML} vs. BP_M, Wilcoxon signed-rank test. Exact F and p values in Suppl. Table 1. Data in Fig. 3f-g are shown as medians ± interquartile ranges.

L6-CT input enhances VPL output to cortex

L6-CT stimulation alone enhanced VPL spiking in the absence of sensory stimulation (Fig. 3), such that high laser intensity evoked spiking in approximately one third of VPL units, and spike output increased as a function of stimulation strength (Fig. S5a), consistent with increased CT output from L6 (Fig. 1). L6 activation also decreased the probability of spontaneous bursting in favor of tonic spiking patterns (Fig. S5b), as reported in the whisker and visual systems [10,14,50], and the extent to which bursting was modulated depended on laser power (Fig. S5b), in line with net depolarization of VPL during sustained CT activation. These increases in both spiking probability and tonic spiking support a scenario in which L6-CT enhances VPL responses to somatosensory stimuli, thereby suggesting a possible neuronal basis for amplified nociception observed in behavior (Fig. 2). To test this hypothesis, we next assessed whether L6-CT activation at moderate laser intensities altered encoding of mechanical stimuli in a paired stimulation protocol (Fig. 3).

Laser stimulation (L) of L6-CT and mechanical stimulation of the paw (M) alone modulated sizable fractions of VPL units (74% and 33%, L and M respectively, Fig. 3b) with substantial overlap between the populations (69% of M-sensitive responded to L, 42% of L-sensitive responded to M), demonstrating that our probes targeted the paw-sensitive region of VPL and that S1 CT projections from ChR2-expressing L6 neurons overlapped with this region (probe location in Supplementary Fig. 4). Paw stimulation alone evoked time-varying responses (Fig. 3d) with diverse profiles, with either phasic responses to initial changes in pressure (dP/dt) during stimulus onset, or less often, sustained responses throughout the duration of the stimulus. The direction of modulation by M relative to baseline was largely positive, in line with the established role of VPL as the main TC path for somatosensory information.

How does L6-CT activation modulate paw responses in VPL? Pairing L6-CT stimulation with paw stimulation (ML) enhanced VPL representation of mechanical stimuli at the population and single-unit levels. In the ML condition, the fraction of responsive VPL units (61%) increased relative to both M and L conditions (33% and 54%, $p < 0.001$, McNemar's test) -- including 12% of previously silent neurons which responded only to this combined condition. At the single unit level, combined ML increased $\bar{r}$, MI, and RP relative to both M and L control conditions (Fig. 3e-h). Estimating from the mean spiking rate and response probability observed across animals, CT activation approximately doubled mechanically-evoked thalamic output on the level of single VPL units (~2 AP/stim vs. 1.5 AP/stim vs 1 AP/stim, for ML, L,

and M conditions, respectively). Aside from enhancing VPL response magnitude and probability, CT activation altered VPL spike timing statistics by shifting mechanically-evoked VPL spiking from burst to tonic mode (Fig. 3i, j). This effect was markedly dependent on baseline firing mode and indeed served to normalize firing modes across units: 1) For units with low bursting probability (BP), L6-CT activation shifted ISIs to lower values (Fig. 3j, dashed lines), reflecting increased firing rates. 2) In contrast, units with higher BP were shifted to tonic mode, as CT activation decreased the fraction of short ISIs (Fig. 3j, solid lines). Thalamic tonic firing patterns likely depolarize cortical targets more effectively because they are less affected by the frequency-dependent depression at TC synapses [51].

Taken together, these findings suggest that the pronociceptive effect of L6-CT activation involves a large thalamic signaling component: under conditions of increased L6-CT activity, baseline feedforward thalamocortical signaling to cortex is increased, suggesting a likely mechanism for the spontaneous pain-like behaviors, as well as enhanced thalamocortical representation of sensory stimuli during paw stimulation underlying hypersensitivity.

Layer-specific modulation of S1 stimulus-evoked responses by L6-CT.

As VPL is the primary thalamic route for somatosensory information to S1HL, we hypothesized that enhancement of thalamic responses by L6-CT could lead to concomitantly enhanced responses in S1 cortex. To test this possibility, we examined depth-resolved spiking in L2/3, L4, L5, and L6 (Methods) during the same stimulation protocol (L, M, ML) used in the VPL recordings (Fig. 4a). Fig. 4b contrasts stimulus-evoked MI at single-unit resolution for the entire pooled population of S1 neurons, showing layer and cell-type-specific responses to mechanical and L6-CT stimulation. Below, we describe the most important comparisons between conditions and layers; complete pairwise comparisons across layers and conditions are summarized in Supplementary Table 2.

Consistent with direct optogenetic control of a large fraction of the L6 population (Fig. 1), the majority (66%) of L6 neurons (Fig. 4b, c, blue shading) were robustly driven in the L condition, with spiking time-locked to the duration of the laser stimulus (Fig. 4d, right). In contrast, L6 units responded weakly to mechanical paw stimulation: only a small fraction (18%) of the L6 population were significantly modulated in M, with only modest MI_M corresponding to low $\bar{r}_M$ and low spontaneous spiking. Indeed, MI_L and MI_{ML} distributions were largely

indistinguishable, suggesting that the majority of responses in the ML condition were laser-evoked only. This is consistent with weak and heterogeneous sensory modulation of L6-CT neurons reported in other sensory cortices [52,53].

Given that L6-CT neurons engage both thalamic and intracortical circuits [7,9,54], we next examined the effect of L6-CT activation on other cortical layers. The degree of suppression and/or enhancement of neuronal responses by L6-CT was highly layer-specific, showing distinct effects on L5 versus L2/3 and L4 (Fig. 4b).

The most striking intracortical effect of L6-CT stimulation was a nearly complete abolishment of spiking in L5 units (Fig. 4b-e, red shading; see Supplementary Table 2 for comparisons across layers). While 51% of L5 units responded robustly to paw stimulation, these responses largely disappeared with L6-CT stimulation. L6-CT stimulation also suppressed spontaneous spiking in L5, with 71% of L5 units negatively modulated (Fig. 4c). From these data, we conclude that while L6-CT stimulation increases VPL output to cortex (Fig. 3), this increased TC input is not sufficient to overcome the intralaminar cortico-cortical suppressive effect, resulting in a predominant suppression of the cortical column, particularly on the L5 population which –aside from L6-CT– constitutes the main output layer of the cortex.

In contrast, the effect of L6-CT activation on upper layers was less extreme (Fig. 4b-e, gray shading). Both L2/3 and L4 showed robust increased spiking in response to paw stimulation, in both proportions of sensory-encoding units (76% and 61%, for L2/3 and L4, respectively; Fig. 4c) and firing rate modulation (Fig. 4d). In contrast to this relative uniformity of sensory encoding, the effect of L6-CT activation was heterogenous and relatively weak, as some units were enhanced or (suppressed) by the laser alone (L): L2/3: 31% (46%), L4: 40% (43%). The combined ML stimulation left the fractions of enhanced/suppressed neurons largely unchanged, but both L2/3 and 4 units showed largely increased $\bar{r}_{ML}$ relative to $\bar{r}_{M}$ (Fig. 4d), although this trend was not significant at the population level for either $\bar{r}$ or MI, likely due to the mixed effects of L6-CT activation. Notably, when units were suppressed by L6-CT activation, they were only rarely entirely silenced. In sum, L6-CT activation weakly enhanced mechanical-evoked spiking of some units in superficial layers, consistent with increased VPL output (Fig. 3), and inhibited spiking of other units, consistent with L6-CT engagement of intracortical inhibition. This moderate net enhancement of superficial layers may contribute to

L6-CT-mediated behavioral hypersensitivity (Fig. 2) during processing of somatosensory stimuli.

Given the marked suppressive effect of L6-CT stimulation on L5 – particularly in contrast to the relatively mild enhancement of superficial layers – and the increasingly established role for L5 neurons in perception as well as pathologies such as chronic pain (reviewed in [38]), we reasoned that this L6–L5 functional interaction may contribute – in synergy with enhanced VPL–S1 TC signaling – to the modulation of pain-like behaviors. To test this hypothesis, we employed cell-type-specific control of L5-PT neurons in behaving mice and studied the function of L5-PT activation on sensitivity, analgesia, and aversion.

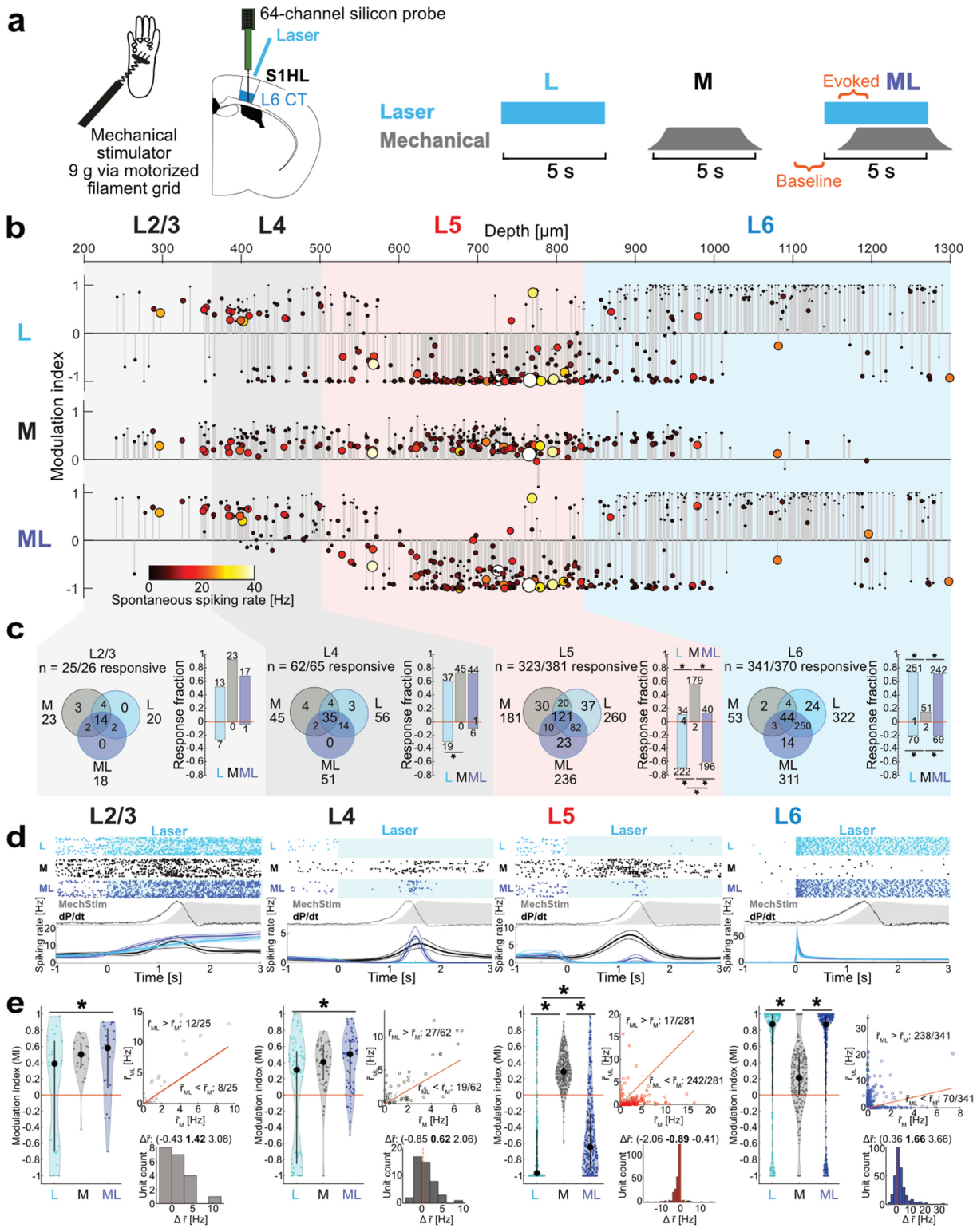
a
64-channel silicon probe
Laser
S1HL
L6 CT
Mechanical stimulator
9 g via motorized filament grid
Laser
Mechanical
L
M
Evoked ML
5 s
5 s
Baseline
5 s
b
L2/3
L4
L5
L6
Depth [µm]
Modulation index
Spontaneous spiking rate [Hz]
c
L2/3
n = 25/26 responsive
L4
n = 62/65 responsive
L5
n = 323/381 responsive
L6
n = 341/370 responsive
Response fraction
d
Laser
MechStim
dP/dt
Spiking rate [Hz]
Time [s]
e
Modulation index (MI)
Unit count
Δ r̄ [Hz]

Fig 4: L6-CT activation suppresses spiking in layer 5 but enhances spiking in superficial layers.

(a) Left: Experimental configuration for layer-resolved silicon-probe recordings in S1HL of anesthetized mice (n = 3). Right: stimulation protocol for three interleaved stimulation conditions: L6-CT activation (L), mechanical paw stimulation (M), and combined L6-CT + mechanical simulation (ML). Time windows for unit spike analysis indicated in orange.

(b) Depth-resolved modulation indices (MI) for L2/3, L4, L5, and L6 units in S1HL for L, M, and ML conditions (top, middle, bottom rows, respectively). Each unit is represented by one data point; size and color of markers are proportional to spontaneous spiking rate (black to yellow: low to high). Depth values are slightly jittered for visibility. Non-significantly modulated units are not shown.

(c) Breakdown of layer-specific population responses to L/M/ML conditions; Left subpanels: Population overlap of L/M/ML - encoding units in each layer. Right subpanels: proportion and counts of enhanced and suppressed units for each L/M/ML condition. For example, ~60% of the L5 units were enhanced by mechanical stimulation (M), while during the ML condition only ~15% were enhanced and ~60% were suppressed. A minority of units had only changes in spike timing, not spike counts (counts at zero).

(c) Example single unit responses for L, M, and ML conditions per cortical layer. Top: raster examples; middle: mechanical pressure (gray shading) and first temporal derivative of pressure (dP/dt, black); bottom: corresponding PSTHs (bin size = 20 ms, smoothed with BARS method [49]).

(e) L6-CT stimulation enhances superficial layers' paw responses, but suppresses those of L5. Left subpanels: Modulation indices pooled per condition and cortical layer. MI_L and MI_{ML} distributions for L6 units were nearly identical ($p = 0.1703$, signed-rank). Upper right subpanels: comparison of $\bar{r}_{ML}$ vs. $\bar{r}_M$ for all units showing significant difference in firing rate between M and ML conditions ($p < 0.05$, signed rank). Lower right subpanels: distribution of $\Delta\bar{r}=\bar{r}_{ML} - \bar{r}_M$ for each unit, negative values correspond to L6-CT-suppressed units and positive values to L6-CT enhanced units. L5 was significantly more suppressed than other layers.

* represents $p < 0.05$; 4c: Chi-squared test followed by Marascuillo procedure, e: Friedman test with post-hoc Wilcoxon signed-rank test. Data in Fig. 3D are shown as medians ± interquartile ranges.

Optogenetically-evoked L5-PT activity in the S1HL cortex reduces mechanical sensitivity and normalizes inflammatory hypersensitivity.

Given our finding that L6-CT stimulation induced (or, in the case of chronic inflammatory pain, worsened) mechanical and thermal hypersensitivity while abolishing L5 spiking, we sought to optogenetically probe the role of L5-PT neurons in eliciting spontaneous nocifensive behavior and modulating hindpaw mechanical sensitivity. To do so, we targeted channelrhodopsin-2-EYFP (ChR2) or EGFP expression to L5 of the right S1HL of Rbp4-Cre mice via stereotaxic injections of AAV-DIO-ChR2-EYFP ("L5-ChR2") or AAV-DIO-EGFP ("L5-EGFP"). Transgene

expression was restricted to L5-PT neurons in S1HL (Fig. 5a EGFP-controls Supplementary Fig. 1a). Silicon probe recordings in anesthetized L5-ChR2 mice validated optogenetic drive of short-latency and low-jitter spiking L5 activity (Fig. 5b) that persisted throughout the 5 second laser stimulus (Fig. 5c).

As with the L6-CT pathway, we asked whether L5-PT activation in S1HL cortex has any measurable effect on spontaneous behavior in fiber-implanted freely-moving animals. At all tested laser intensities (0-318 mW/mm²), none of the L5-ChR2 animals showed optogenetically-elicited nocifensive behavior, in stark contrast to the observations in the L6-ChR2 animals (Fig. 5 d, Supplementary video 2).

How does L5-PT activation modulate paw sensitivity? Quantification of mechanical sensitivity using the Von Frey test revealed that L5-PT activation significantly decreased mechanical sensitivity over nearly the entire range of tested mechanical forces (Fig. 5e), but remained unchanged in L5-EGFP control animals (Supplementary Fig. 2a). Thus, in contrast to L6-CT stimulation (Fig. 2b), L5-PT stimulation decreased mechanical sensitivity, suggesting an anti-nociceptive function of the L5-PT pathway. To test this directly, we repeated the mechanical sensitivity measurements in the CFA inflammatory pain model. In CFA-injected L5-ChR2 animals, laser stimulation of the S1HL decreased mechanical sensitivity (Fig. 5f), an effect not present in L5-EGFP control animals (Supplementary Fig. 2i). These effects were also observed when computing filament force thresholds that elicited paw withdrawal in 60% of trials, in addition to revealing that L5-PT stimulation returns mechanical sensitivity in CFA-injected animals back to pre-CFA sensitivity, suggesting that L5-PT stimulation can normalize inflammation-induced hypersensitivity (Fig. 5g).

Examining the putative L5-PT modulation of thermal sensitivity using Hargreaves test, we did not observe statistical differences between the tested groups (Fig. 5h). The lack of S1 L5PT modulation of heat sensation is in line with recent findings of segregated thermal pathways in which S1 is not involved in encoding warmth [55,56].

We had observed that L6-CT activation causes pronounced negative affective responses (Fig. 2 h-j) and asked whether L5-PT activation in S1HL cortex has comparable effects. Repeating the real-time conditioning paradigm (CPA) from Fig. 2 but with L5-PT stimulation, we found that L5-ChR2 mice spent less time in the chamber paired with optogenetic stimulation relative

to the time spent in the same chamber during the baseline session (i.e. without optogenetic stimulation) (Fig. 5i, j). However, the avoidance in L5 ChR2 animals was much less pronounced compared to L6 ChR2 animals (Fig. 2 h-j) and may arise entirely from visual aversion to the laser flashes. Indeed, inspecting the control animals in both groups (L6-EGFP and L5-EGFP, Fig. 2i, 5j) reveals a significant trend to avoid the laser-stimulated chamber, suggesting that laser light reaching the retina contributes to the aversive effect independently of the somatosensory system. In line with this observation, analyses of the preference indices show that laser stimulation in S1HL in both L5-ChR2 and L5-EGFP controls caused comparable avoidance for the laser paired chamber. Furthermore, in both cases, the effect was too small to result in an overall preference reversal for the unpaired chamber (Fig. 5k), which is in stark contrast to L6-ChR2 animals, whose preferences switched to the unpaired chamber (Fig. 2j). We conclude that L5-PT activation is much less aversive, if at all, compared to L6-CT activation.

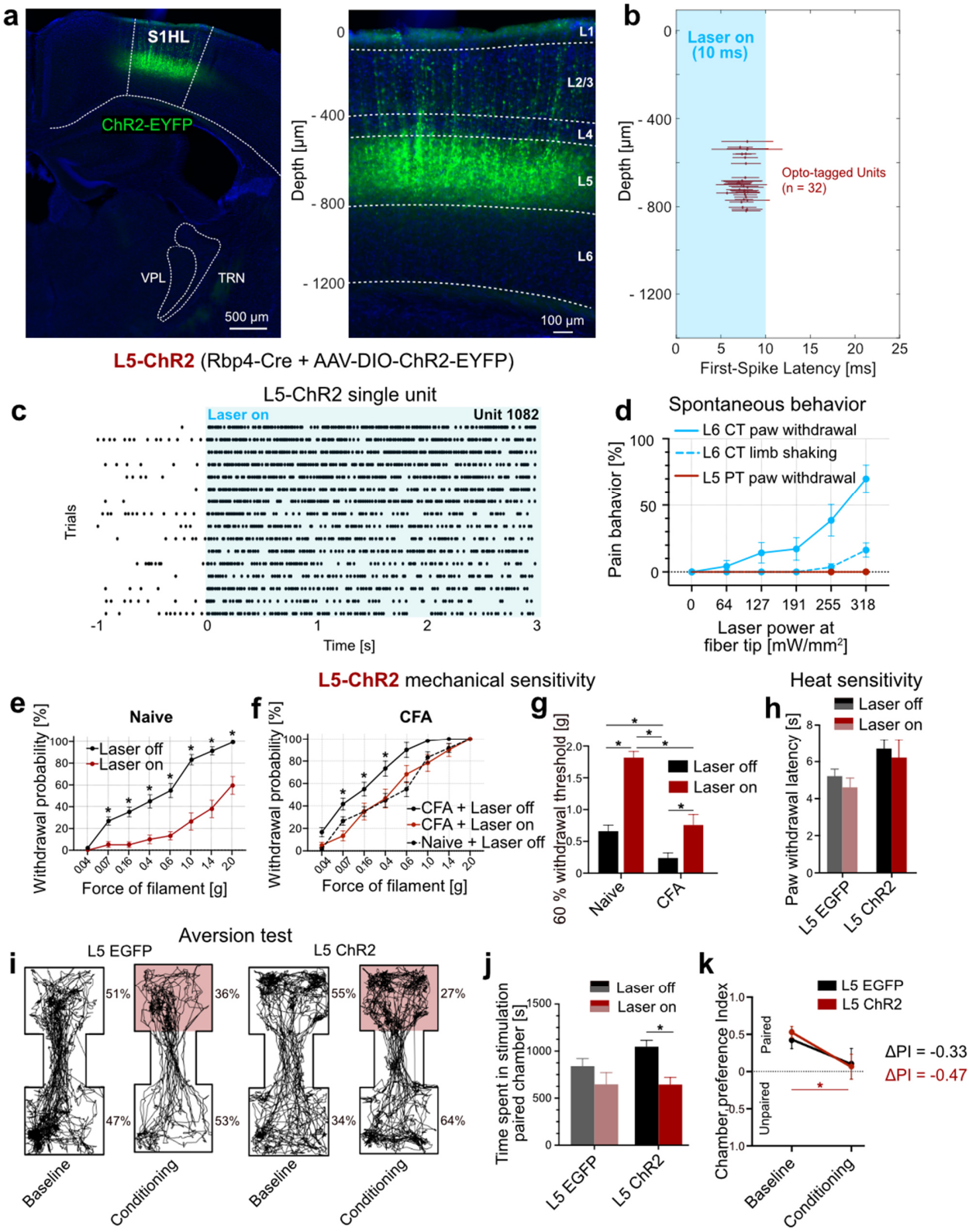
a
S1HL
ChR2-EYFP
VPL
TRN
500 µm
Depth [µm]
L1
L2/3
L4
L5
L6
100 µm
b
Laser on
(10 ms)
Opto-tagged Units
(n = 32)
First-Spike Latency [ms]
L5-ChR2 (Rbp4-Cre + AAV-DIO-ChR2-EYFP)
c
L5-ChR2 single unit
Laser on
Unit 1082
Trials
Time [s]
d
Spontaneous behavior
L6 CT paw withdrawal
L6 CT limb shaking
L5 PT paw withdrawal
Pain bahavior [%]
Laser power at
fiber tip [mW/mm²]
L5-ChR2 mechanical sensitivity
e
Naive
Laser off
Laser on
Withdrawal probability [%]
Force of filament [g]
f
CFA
CFA + Laser off
CFA + Laser on
Naive + Laser off
g
60 % withdrawal threshold [g]
Naive
CFA
h
Heat sensitivity
Paw withdrawal latency [s]
L5 EGFP
L5 ChR2
Aversion test
i
L5 EGFP
L5 ChR2
51%
36%
55%
27%
47%
53%
34%
64%
Baseline
Conditioning
j
Time spent in stimulation paired chamber [s]
k
Chamber preference Index
Paired
Unpaired
ΔPI = -0.33
ΔPI = -0.47

Fig. 5: Optogenetically-evoked L5 activity in the S1HL cortex decreases mechanical sensitivity and normalizes inflammatory allodynia.

(a) Expression of ChR2-EYFP (green) in S1HL of a L5-ChR2 mouse showing fluorescence in L5-PT neurons. Magnification of S1HL cortex (right panel) with L5-PT neurons depth-registered relative to S1HL layer borders (dashed lines, estimated based on soma sizes and densities using DAPI signals, blue).

(b-c) Representative S1HL cortex silicon probe recording from a L5-ChR2 mouse demonstrating specific optogenetic control of the L5-PT pathway. **(b)** L5-PT units were identified based on their short-latency, low jitter response to 10 ms light pulses (1201 mW/mm²). Each marker shows unit depth vs. mean ± SD latency to first evoked spike (n = 32 out of 203 units recorded at the depth of L5). **(c)** Raster plot depicting time-locked, persistent S1HL L5-PT spiking evoked by laser stimulation (1201 mW/mm^2).

(d) Quantification of L6-CT-evoked behaviors (blue, n = 11) and the absence thereof for L5-PT stimulation (red, n = 6); paw lifting (solid line) and limb shaking (dashed line). See also Supplementary video 2.

(e) Within-animal comparison of paw withdrawal probabilities in response to graded von Frey stimulation of the hindpaw at baseline (black, laser off) and during laser stimulation (red, laser on, 5 s continuous pulse) in the contralateral S1HL of L5-ChR2 mice (n = 6). L5-EGFP control animals in Supplementary Fig. 2a.

(f) Same as in **(e)** but after animals were injected with CFA in the left hindpaw to induce paw inflammation (n = 12). For comparison of pre- and post-CFA withdrawal probabilities see Supplementary Fig. 3.

(g) Comparison of filament forces that evoked paw withdrawal in 60% of the stimulation trials as a function of L5-PT activation without (Naive) and with (CFA) inflammation (n = 7). Higher filament forces indicate decreased sensitivity.

(h) Paw withdrawal latencies in response to heat stimulation of the left hindpaw with (Laser on, red, 5 s continuous pulse) and without (black, Laser off) optogenetic stimulation of L5-PT in the contralateral S1HL of L5-EGFP (n = 7) and L5-ChR2 (n = 7) mice.

(i) Example animal tracking plots from L5-EGFP and L5-ChR2 mice, recorded at baseline and during conditioning with 20 Hz laser stimulation of the S1HL cortex; area highlighted in red indicates the laser-paired chamber; mice received no stimulation in the other chamber. Percentages show relative time spent in each chamber.

(j) Population analysis of total time spent in the laser-paired chamber at baseline (Laser off, black/gray) and during stimulation (Laser on, red 20 Hz laser stimulation in S1HL cortex) of L5-EGFP (n = 7) and L5-ChR2 (n = 7) mice.

(k) Average chamber preference indices (PI) for L5-ChR2 (n = 7) and L5-EGFP (n = 7), computed for the last baseline session and the first stimulation session. A PI of 1 indicates a full preference for the paired chamber, while a PI of -1 indicates a full preference for the unpaired chamber.

* represents $p < 0.05$; 5e-j: Repeated measures ANOVA with post-hoc Bonferroni test, k: L5 CPA preference indices, Repeated measures ANOVA with post-hoc Bonferroni test; L5 CPA change in preference indices, one-tailed unpaired t-Test. Exact F and p values in Suppl. Table 1. Data are shown as mean ± S.E.M.

S1 bidirectionally modulates paw sensitivity via L6-CT and L5-PT in a frequency-dependent manner.

We next directly compared the effects of L5-PT and L6-CT stimulation across animals and stimulation forces, illustrating that L5-PT reduces sensitivity and L6-CT increases sensitivity for a given mechanical stimulation force (Fig. 6a).

As a single readout for overall mechanical sensitivity, we computed areas under the curves (AUC) from all mechanical sensitivity measurements, which allowed us to directly compare the modulatory functions of cortical pathway-specific optogenetic stimulation on sensitivity in the naive and CFA-inflamed mouse model. Compared to baseline levels (Laser off), high AUC values correspond to hypersensitivity and were caused by L6-CT stimulation and by paw inflammation in CFA animals. In contrast, low AUC values indicate reduced sensitivity and were caused by L5-PT stimulation (Fig. 6b), demonstrating that L6-CT and L5-PT in S1 can modulate paw sensitivity in opposite directions (Fig. 6c).

Both L5 and L6 corticofugal synapses have well-established frequency-dependent short-term plasticity, with distinct functional impact on thalamocortical signal processing [14,57]. For instance, it has been shown that L6-CT can depress or excite thalamic neurons, depending on the frequency of L6-CT synaptic activity [14]. To assess whether short-term synaptic plasticity could have an effect at the level of behavior and in a perceptual context, we probed sensitivity as a function of stimulation frequencies applied to L5-PT and L6-CT neurons (1 Hz, 2 Hz and 20 Hz, Fig. 6d). We found that mechanical sensitivity changed with stimulation frequency and in opposite directions, depending on the stimulated CT pathway, with L5 excitation decreasing and L6 stimulation increasing mechanical sensitivity (Fig. 6e). AUC calculations of this data (Fig. 6f) directly illustrate the bidirectional frequency-dependence, with higher frequencies resulting in stronger behavioral changes.

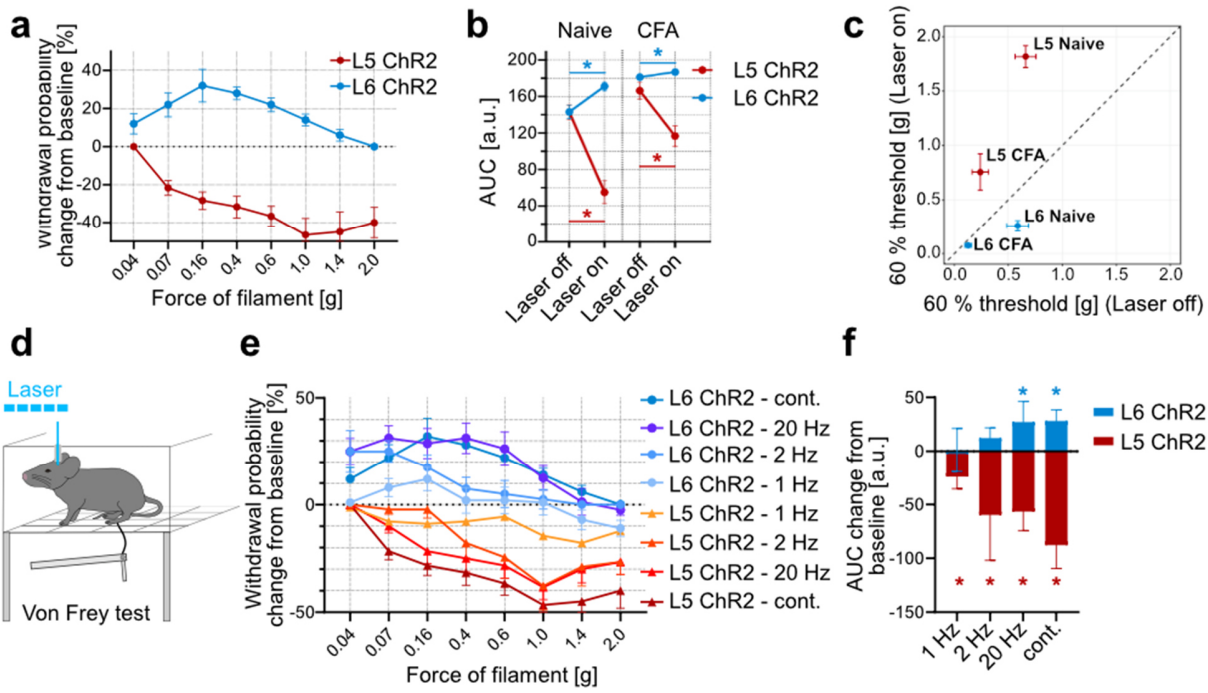

Fig. 6: Bidirectional modulation of sensory gain and nociception via S1 L6-CT and L5-PT.

(a) Withdrawal probabilities during L5-PT (red, n = 6) or L6-CT (blue, n = 10) optogenetic stimulation (5 s continuous laser above S1HL) as a function of filament force, expressed as changes from baseline measurements (stippled line, Laser off trials).

(b) Comparison of mechanical sensitivity, computed from areas under the curves (AUC) from naive and CFA-inflamed mice, with (Laser on) and without (Laser off) activation of L5-PT and L6-CT neurons in S1HL. Increased AUCs correspond to increased sensitivity (hypersensitivity) and decreased AUCs correspond to decreased sensitivity (hyposensitivity). L5-PT n = 9; L6-CT n = 10.

(c) Comparison of filament forces that evoked paw withdrawal in 60% of the stimulation trials measured in naive and CFA-inflamed mice with (Laser on) and without (Laser off) activation of L5-PT (n = 24) and L6-CT (n = 21) neurons in S1HL. Data points below the diagonal (dashed line) correspond to increased sensitivity (hypersensitivity) and above correspond to decreased sensitivity (hyposensitivity).

(d) Schematic of Von Frey setup to probe the relationship between mechanical sensitivity and optogenetic stimulation of L5-PT and L6-CT at different stimulation frequencies.

(e) Same as in **(a)** but for different L5-PT and L6-CT stimulation paradigms: 1, 2, 20 Hz and continuous (cont.) laser pulses, revealing that L5-PT and L6-CT effects scale with stimulation frequency.

(f) Comparison of mechanical sensitivity, computed from relative changes of the areas under the curves (AUC) with (Laser on) and without (Laser off) activation of L5-PT and L6-CT in S1HL at different frequencies.

* represents $p < 0.05$; 6b, f: Repeated measures ANOVA with post-hoc Bonferroni test. Exact F and p values for all statistical tests are given in Suppl. Table 1. Data are shown as mean± S.E.M.

Discussion

Pain is an inherently context-dependent phenomenon. Competing needs, psychosocial factors, and cross-modal sensory interactions can exacerbate or ameliorate the subjective experience of pain [15,58,59] and such contextual effects point to central neural mechanisms for "top-down" control over pain perception. Here, we investigated how two distinct top-down pathways from the S1HL cortex modulate somatosensation in behaving mice, revealing that L6-CT activity not only increases somatosensory sensitivity but also evokes aversion and nocifensive behavior, whereas L5-PT activity has largely an opposing, antinociceptive effect. This bidirectional control of pain-related behaviors was frequency-dependent, and effective in both acute and inflammatory pain models.

The robust aversive effects of L6-CT were unexpected, as existing research has primarily studied L6-CT in purely sensory contexts and left unresolved how L6-CT functions link to subjective sensory experiences and to the modulation of behavior. It is broadly established that L6-CT pathways endow sensory systems with 'beneficial' information processing functions, such as controlling sensory gain [7,8,11,54,60], tuning selectivity, and mediating burst-tonic transitions in the thalamus [10,12,61]. Such sensory functions for L6-CT neurons have not yet been revealed in the S1 hindlimb cortex. Our observation that S1HL L6-CT activation enhances paw sensitivity over a range of thermal and mechanical stimulation strengths is in line with L6-CT gain control functions described in other modalities. However, the results presented here go further and expand the function of L6, suggesting that, contingent upon L6-CT output level, gain control follows a functional continuum spanning both increased sensitivity and aversive hypersensitivity, even exacerbating preexisting hypersensitivity in inflammatory pain and triggering spontaneous pain-like behavior absent sensory stimulation.

What are the possible circuit mechanisms underlying L6-CT-mediated hypersensitivity? To disentangle corticothalamic [1,10,14] and cortico-cortical effects [8,9,42] of L6-CT activation, we made silicon probe recordings in VPL and S1 and assessed how L6-CT activity modulates thalamocortical representations of mechanical stimuli. We found that L6-CT enhances VPL spiking and modulates S1 in a layer-specific manner.

Notably, the VPL recordings revealed several parallel mechanisms favoring increased thalamocortical sensory transmission. L6-CT activation not only enlarged the fraction of sensory-encoding units in the thalamus, but also increased spike output on the level of individual units, and in parallel, both favored tonic spiking mode and inhibited non-responding units. Taken together, these effects support an enhanced signal-to-noise ratio of sensory output to the cortex. Interestingly, in addition to providing the major thalamic input to S1, VPL also projects to the posterior insular cortex [62], opening the possibility that increased VPL-posterior insular cortex contributes to L6-CT-mediated aversion. Our findings suggest that L6-CT is a central pathway to modulate VPL excitability with the potential to induce aversion and not just increase sensory sensitivity.

At the cortical level, the most salient effect of L6-CT stimulation was a nearly complete suppression of L5 neurons' spontaneous and sensory-evoked spiking. This suppression likely comes about from L6-CT recruitment of translaminar inhibitory circuits shown in the barrel and visual cortices [7–9,54]. This strong suppressive effect of L6-CT on L5 neurons led us to hypothesize an opposing role for L5-PT neurons in modulating somatosensation, revealing that L5-PT stimulation reduced sensitivity, and reversed inflammatory allodynia. While this finding points to an antinociceptive effect of L5, other studies have focused on L5 hyperexcitability and bursting in pain states [39,63,64], which could reflect compensatory top-down mechanisms to control pain. Based on the corticothalamic anatomy of the S1 limb area [6], this antinociceptive action of L5 is unlikely to involve VPL, but rather subcortical L5-PT target circuits – e.g., posterior medial thalamus, zona incerta, periaqueductal gray or spinal cord– several of which have been associated with pain [40,65–67]. Untangling the downstream effects of L5-PT stimulation may generate valuable interventional strategies for pain management.

Behavioral determinants and circuit mechanisms controlling L6-CT activity are only beginning to be studied, let alone those that potentially lead to L6 hyperactivity or synchronization. Both human and animal studies have demonstrated a link between cortical synchronization and pain states [28,68]. Broadly speaking, high levels of cortical synchrony are correlated with pain states, and strong cortical synchronization triggered by gamma entrainment of S1 induces a nociceptive state [29] that is similar to the effects of L6-CT activation reported here. Optogenetic stimulation tends to synchronize neuronal activity, which likely helped to uncover adverse effects of CT gain control in this study. These findings also raise considerations for studies investigating L6-CT and L5-PT pathways with opto- or chemogenetic interventions. In

particular, study design should factor in potential aversive effects unintentionally evoked by L6-CT manipulations, especially in sensory cortices for which motivational or affective effects might not be obvious considerations.

In conclusion, this study reveals dual modulation of sensitivity and nociception via two specific populations of cortical output neurons in S1, underscoring the potential of corticofugal pathways as therapeutic targets. The role of S1 in pain has been debated[31], as targeting S1 has been shown to both beneficially alter pain trajectories but also enhance nociceptive responses [26,27,29,39,69]. Moreover, previous causal studies affected bulk S1 activity across all layers and cell types and were thereby unable to functionally disambiguate the opposing roles of the two cortical output pathways, contributing to the view that S1 is not involved in pain affect. The data presented here provide clarifying insights into the nociceptive role of S1 which were only possible by layer-specific manipulations and analysis of intracortical and cortico-thalamic interactions as functional determinants of behavior and perception. Understanding how the balance of corticofugal output is maintained in health and altered in disease is a promising direction for future studies.

Methods

Animals

Mice (male and female, 7-16 weeks of age) were housed with food and water *ad libitum* on a 12h light/dark cycle. All experimental procedures were performed according to the ethical guidelines set by the governing body (Regierungspräsidium Karlsruhe, Germany).

Mouse lines

Layer 6 optogenetic stimulation:

"Ntsr1-Cre" (B6.FVB(Cg)-Tg/(Ntsr1-cre)GN220Gsat/Mmucd)

"Ntsr1-Cre-ChR2-EYFP"; crossbreed between "Ntsr1-cre" x "Ai32" (B6.FVB(Cg)-Tg/(Ntsr1-cre)GN220Sat/Mmucd x B6.129S-Gt(ROSA)26Sortm32(CAG-COP4*H134R/EYFP).

Layer 5 optogenetic stimulation:

"Rbp4-Cre" (B6.FVB/CD1-Tg(Rbp4-cre)KL100Gsat/Mmucd)

Virus injection and optical fiber implantation

Ntsr1-Cre and Rbp4-Cre mice were stereotaxically injected with either an excitatory opsin (AAV2-EF1a DIO-ChR2(H134R)-EYFP-WPRE-pA, Zürich vector core) or a control virus (AAV2-hSyn-DIO-EGFP, Addgene). A subset of the optogenetic L6 experiments was done in Ntsr1-Cre-ChR2-EYFP mice, which were not virus injected. We observed no differences in any of the measurements and pooled Ntsr1-Cre-ChR2-EYFP mice and virus injected Ntsr1-Cre experiments.

Mice were placed in a stereotaxic frame (Kopf Instruments) and anesthetized with 1.2-2.0 vol % Isoflurane in medical oxygen at a flow rate of 0.8 L/min, while keeping body temperature at 39°C. Carprofen (CP-Pharma) was administered subcutaneously (5 mg/kg) and Lidocaine (Xylocain 1%, Aspen Pharma) was injected under the scalp and around fixation ear bars for local anesthesia. Eyes were covered with Bepanthen ointment (Bayer) to prevent eye drying during the surgery. After ensuring the absence of tail and toe pinch reflexes, skin was opened with a midline incision, the periosteum and aponeurotic galea was removed to visualize anatomical reference points (bregma and lambda), and the head was aligned to the stereotaxic frame. Small craniotomies were drilled above the S1HL area and viral particle solutions were injected into two sites within S1HL with calibrated glass micropipettes (Blaubrand; IntraMARK) at the following coordinates relative to bregma (AP, ML) and pia mater (DV):

First injection: ML= +1.4 mm, AP = -0.46 mm; second injection: ML= +1.5 mm, AP = -0.94 mm. Ntsr1-Cre mice were injected at a depth of -0.9 and -1.0 mm, while Rbp4-Cre mice were injected at a depth of -0.7 and -0.8 mm (100 nl at each depth, followed by a waiting period of 10 minutes before relocating the injecting pipette).

Chronic optical fiber implants (200 µm diameter, numerical aperture of 0.39, Thorlabs GmbH) were placed on the dura above the S1HL (ML = +1.5 mm, AP = -0.94 mm), and the ceramic

ferrule encapsulating the optical fiber was fixed to the skull with dental cement. Mice were kept between three and four weeks for optimal viral expression before experiments.

Histology and immunohistochemistry

The mice were sacrificed by transcardial perfusion with 4% paraformaldehyde (PFA) in PBS. The brains were sectioned with a vibratome (Thermo Scientific Microm HM 650 V) at a thickness of 80 µm. Selected sections were stained with DAPI, mounted with Mowiol and imaged with an epifluorescent microscope (Leica DM6000).

Behavior

Behavioral experiments were conducted during the light cycle and experimenters were blinded to the experimental identity of the animals.

Optogenetic stimulation

The implanted fiber was coupled to an optical patch cord (Thorlabs GmbH) attached to a laser output module (473 nm) (Shanghai Laser Optics Century Co., Ltd.). The laser power at the fiber tip was measured with a power energy meter (Thorlabs GmbH). Irradiance values for layers 5 and 6 were estimated based on previous measurements in mammalian brain tissue [70]. For 10 mW measured at the fiber tip (fiber NA = 0.39; fiber radius = 100 µm), the irradiance is 318.18 mW/mm², which corresponds to 3.47 mW/mm² at the level of L5 (0.75 mm cortical depth) and 1.54 mW/mm² at the level of L6 (1 mm cortical depth).

Laser protocols

Single laser pulse trials were 5 s long and consisted of continuous laser stimulation or pulsed trains (1, 2, 20 Hz, pulse length = 20 ms). Mechanical and thermal stimuli were applied during laser pulses. Optical stimulation blocks were interspersed with 30 s non-stimulation blocks.

Measurements to determine individual paw lifting laser intensity thresholds

Laser stimuli (5 s continuous) were applied at 10, 8, 6, 4, 2, 0 mW (318.18 254.55, 190.91, 127.27, 63.64, 0 mW/mm²) five times at each intensity and paw lifting probabilities were calculated for each intensity (Fig. 1E). For each mouse, we determined the highest intensity resulting in a lack of paw lifting and used this individual laser intensity during sensitivity measurements (mechanical and thermal).

Inflammatory pain model

20 µl of Complete Freund's adjuvant (CFA) was subcutaneously injected into the left hindpaw under anesthesia using isoflurane.

von Frey test

Mice were habituated to the von Frey test chamber twice a day for 1 h for three consecutive days without von Frey filament stimulation. Each von Frey test session started with an acclimatization period of 15 min. Mechanical sensitivity was quantified as the probability of paw withdrawal in response to the application of von Frey filaments (Aesthesio Precise Tactile Sensory Evaluator, Ugo Basile S.R.L.) to the plantar surface of the left hindpaw (contralateral to the stimulated HL cortex). Eight filaments (0.04-2.0 g of force) were applied five times each

in ascending order, with at least 30 seconds delay between applications. 100% withdrawal probability was reached when one filament provoked a withdrawal response in all 5 trials. In this case, measurements were stopped and sensitivity for filaments with greater forces was not tested. Mechanical sensitivity was first measured in the absence of laser stimulation (baseline) and, after approximately one hour in the homecage, the test was repeated with laser stimulation of either S1HL L6-CT or L5-PT pathways. Another round of tests (baseline and laser) was conducted one day after subcutaneous injection of Complete Freud's adjuvant (CFA) in the left hindpaw.

Thermal test

Thermal sensitivity was tested using the Hargreave's setup (Ugo Basile Inc., Italy) equipped with an infrared heat laser (Model 37370-001, Ugo Basile). The heat laser was aimed at the plantar surface of the left hindpaw and produced radiant heat of increasing intensity. The intensity level was set to 35 and the cut-off time to 20 s to avoid damage to the paw. Three heat stimulation trials were applied alone, and then in the presence of optogenetic laser stimulation (238.64 mW/mm²), with 3 min of recovery time between trials. The paw withdrawal latency was measured per trial.

Conditioned place aversion (CPA) test

The setup for this paradigm consisted of two chambers (each 15 cm x 15 cm) separated by a neutral chamber (8 cm x 8 cm). One chamber contained walls with vertical stripes and a cherry scent, while the other chamber contained walls with horizontal stripes and a honey scent. The paradigm consisted of five baseline sessions followed by two conditioning sessions, each lasting 20 minutes. Prior to each session, animals were lightly anesthetized with isoflurane and were attached to an optic fiber cable, at which point they were restricted to the neutral chamber using removable wall slides. Once recovered from anesthesia, the wall slides were removed and the session was started. During baseline sessions, no optogenetic stimulus was administered. During the conditioning sessions, optogenetic stimulation (8 mW, 254.55 mW/mm^2, 20 Hz) was administered when the animal entered the chamber in which it had spent less time in the last baseline session. Pulsed stimulation at 20 Hz was chosen to reduce phototoxic effects during prolonged stimulation required for the CPA paradigm. AnyMaze software (Stoelting Co., Ireland) was used to track the animals' position and time spent per chamber for every session. To assess performance outcomes, a comparison was made between the time spent in the preferred chamber during the last baseline session and the time spent in that same chamber during the last conditioning session. Preference indices (PI) were computed using the following formula: (time in paired chamber - time in unpaired chamber)/(time in paired chamber + time in unpaired chamber).

Statistics and Data Analysis

All behavioral data are expressed as the mean ± the standard error, and were analyzed using SPSS and R. Unless stated otherwise, two-way ANOVA for repeated measures with Bonferroni tests for multiple comparisons were used. A *p*-value less than 0.05 was considered to be significant. Microscopy images were edited using Fiji/Image J. Schematics and figures were created in Affinity Designer, GraphPad Prism (Version 9.1.1), and Matlab 2022a.

Electrophysiology

Mice were anesthetized using urethane (1.4 g/kg, i.p.) and maintained using an oxygen-isoflurane mixture (0.2%). The mice were fixed with ear bars and the skull was leveled. A craniotomy was performed above the recording site, and a well was cemented (Paladur) and filled with isotonic Ringer's solution. Sharpened 64-channel silicon probes (impedance ~50 kOhm) (Cambridge Neurotech) were inserted into the S1HL cortex (ML = +1.67 mm, AP = -1.0 mm, DV = -1.4 mm) or VPL (ML = +1.8, AP = -1.3, DV = -4.5) using a micromanipulator (Luigs Neumann 3-axis Motor), moving at ~2 µm/s. The probes were docked to a connector (ASSY-77) with an adaptor (A64-Om32x2 Samtec) that was in turn connected to a RHD2164 headstage amplifier chip (Intan technologies). Signals were amplified and digitized at a sampling rate of 30,030 Hz via an RDH2000 Intan evaluation board using USB 2.0 interface. An Intan Talker module (Cambridge Electronic Devices, Cambridge, UK) was for data acquisition with Spike 2 (v9.06) software.

Mechanical stimulation

Target regions were identified by brushing or pressing the hindpaw with a brush or cotton swab and assessment of evoked activity from the Spike 2 visual interface readout. Mechanical stimulation was automated by a stimulation protocol prepared in Spike2 through an interface hardware (Power1401, Cambridge Electronic Design, Cambridge, UK) through a stepper controller, which initiated a motor (Mercury Step C-663 Stepper Motor Controller, PIcroMove). Nine Von Frey filaments glued (Pattex Sekundenkleber) to a force sensor (Single Tact miniature force sensor) attached to a motor, so the TTL pulse would apply these Von Frey filaments to the paw, and pressure information would be relayed to the Intan board. A total 9 g (9 x 1 g per filament) pressure was delivered for 5 s duration every 60 seconds (based on protocol in Hohmmann et al., 1995; Martin et al., 1996).

Optogenetic stimulation

An optical fiber (Thorlabs GmbH, NA = 0.22; radius = 52.5 µm) was positioned ~0.5 mm perpendicular above the craniotomy. Laser power densities overlapped with the behavioral experiments (~0.5 - 27 mW at fiber tip corresponding to 57.72 - 3105.34 mW/mm² and 0.26 - 14.16 mW/mm² at the level of L6 [70]). Light pulses were initiated automatically by a stimulation protocol prepared in Spike2 through an interface hardware (Power1401, Cambridge Electronic Design, Cambridge, UK). Trial repetitions per condition were 31-52 trials for VPL recordings and 32-35 trials for S1 recordings.

Stimulation protocol

Experiments consisted of three stimulus conditions of 5 seconds duration each: mechanical, mechanical + optogenetic laser, and optogenetic laser. The time interval between mechanical and mechanical + optogenetic laser conditions was 60 seconds, otherwise the time interval between conditions was 30 seconds (Figure 3A).

Spike Sorting

Voltage data were band-pass filtered (500-5000 Hz). Spike2 data files (.smrx) were converted into binary files. The file conversion consisted in reading the electrophysiology channels in the

.smrx file, transforming them back into uint16 values from the 16-bit depth analog-to-digital (ADC), and writing them in the resulting .bin file.

Spike sorting was performed semi-automatically using Matlab-based Kilosort 2.5 [71] and resulting clusters curated in Phy2 cite. Single units with <0.5% refractory period (1 ms) violations and a baseline spike rate >0.1 Hz were accepted for further analysis. Kilosort 2.5 spike-sorting parameters were:

Parameter	Value	Parameter	Value
ops.fs	3.003003003003003 e+04	ops.sigmaMask	30
ops.fshigh	600	ops.ThPre	8
ops.Th	[10 2]	ops.sig	20
ops.lam	10	ops.nblocks	0
ops.AUCsplit	0.7	ops.spkTh	-6
ops.minFR	1/50	ops.reorder	1
ops.momentum	[20 400]	ops.nskip	35
ops.GPU	1	ops.Nfilt	1024
ops.nfilt_factor	4	ops.ntbuff	64
ops.NT	64*1024+ ops.ntbuff	ops.whiteningRange	32
ops.nSkipCov	25	ops.scaleproc	200
ops.nPCs	6	ops.useRAM	0

Classification of putative cell types

VPL units:

VPL units were defined as follows. First, probe location within VPL was confirmed histologically (Fig. S4): For each recording we first identified the dorso-lateral range of channels which contained units with significant responses to M or ML. All units within that range were assigned to VPL.

Cortical units:

Silicon probe recording channels were registered to histological layer borders to assign each unit a cortical depth and layer. Layer borders in S1HL cortex were estimated histologically, based on soma sizes and densities using DAPI signals (examples in Figs. 1, 5). L6-CT and

L5-PT units were identified further based on their increased spike rate in response to laser stimulation (Figs. 1, 5)

Spike train analysis

After spike-sorting, spike times were aligned to stimulus onsets and segregated into stimulation conditions using custom Matlab 2022a scripts. For cleaner visualization in Figs. 3 and 4, peristimulus time histograms (bin size = 20 ms) were smoothed using a Matlab port (https://github.com/iandol/spikes/tree/master/Bars) of the Bayesian Adaptive Regression Splines technique [49] using default parameters except for prior_id = 'POISSON'. All further calculations were done on unsmoothed data.

Response windows

We considered spike counts and timing within a time window of 1.5 seconds after the stimulus onset + 500 ms to account for delayed activation of the mechanical stimulus relative to the command signal and baseline activity was taken as 1.5s before stimulus onset (Figs. 3a and 4a). Laser-only trials were also sampled during the same windows to discard transient effects at stimulus onset (e.g. PSTH peak in Fig. 4d, L6) and to enable comparison between L and ML conditions.

Unit modulation

Units were considered modulated in a given stimulus condition if a significant difference was measured between baseline and stimulus-evoked spiking either in terms of absolute spike counts ($p<0.05$, signed-rank test for paired baseline and stimulus-evoked trials) or spike timing detected by using the ZETA test [72].

Response parameters

We compared stimulus-evoked changes in single unit activity across L, M, and ML conditions using spike counts and interspike interval (ISI) statistics to capture both overall spike output and spike timing. Mean spiking rate ($\bar{r}$) was calculated as the mean spike count per trial, divided by the response window duration of 1.5 s. Response probability (RP) was calculated as (trial count with at least one spike)/total trial count, measured within the 1.5 s response window.

To calculate burst probability (BP) for single units, spikes preceded by an interspike interval of less than 5 ms were considered part of a burst. BP was then calculated as total burst events/(total burst events + total single spike events). Trends reported were relatively insensitive to a burst cut-off ISI of up to 10 ms. Modulation index (MI) was calculated as MI= $(\bar{r}_{stimulus}-\bar{r}_{baseline})/(\bar{r}_{stimulus}+\bar{r}_{baseline})$ as in [73]. Data are presented as (first quartile, median, third quartile) or mean ± S.E.M.

Statistical analysis of spike train data

All statistical analysis was done in Matlab 2022a or R, using built-in or custom-written functions. Unless otherwise stated, data was analyzed by two-way repeated measures ANOVA with a Bonferroni correction. See Supplementary Table 1 for exact statistical tests

and test outputs (F- and p-values). Paired MI and r̄ data across conditions (per region) were analyzed using the Friedman test, followed by a Wilcoxon signed-rank test. MI and r̄ comparisons across regions (Supplementary Table 2) was done with a mixed-model ANOVA followed by a rank-sum test for pairwise differences. Comparisons of proportion of either positively, negatively, or unmodulated units per stimulation condition were made by a X^2 proportions test, followed by the Marascuillo procedure for multiple comparisons. Statistical differences in the proportions of responsive units across conditions were assessed using McNemar's test in the case of paired data or a two-proportions X^2 test in the case of unpaired data (custom written), e.g. between cortical layers.

Data availability

All the data are in the manuscript or in supplementary material. Source data will be made available in the following link: HeiDATA (https://heidata.uni-heidelberg.de/)

Code availability

Codes used in this study are available upon request and will be provided under the following link: Github

Author contributions

Conceptualization: AG, RM
Methodology: SAG, JMC, LT, SK, RK, TK
Investigation: KZ, JB, RF, AJG
Data analysis and analysis tools: KZ, JB, RF, AJG, EIC, RM
Visualization: KZ, JB, RF, AJG, RM, AG
Funding acquisition: AG, RM, RK, TK
Project administration: AG, RM
Supervision: AG, RM, RK, TK
Writing – review & editing: KZ, JB, RF, AJG, EIC, JMC, RK, TK, RM, AG

Acknowledgments

The authors are grateful for technical assistance from Manfred Oswald and Zheng Gan, and software development and support from Liam Keegan (Scientific Software Center, Heidelberg University).

Funding

Funding by the Deutsches Forschungsgemeinschaft in Collaborative Research Center 1158 (AG & RM: project B10; RK: project B01, B06; TK: project B08). Chica and Heinz Schaller Stiftung and the Brigitte-Schlieben-Lange Programm by the Ministry of Science, Research and the Arts Baden-Württemberg (RM). The authors gratefully acknowledge the High Performance Computing in Baden-Württembergand data storage service SDS@hd supported by the Ministry of Science, Research and the Arts Baden-Württemberg (MWK) and the

German Research Foundation (DFG) through grant INST 35/1314-1 FUGG and INST 35/1503-1 FUGG.

Conflict of interest

Authors declare that they have no competing interests.

References

1. Born, G. *et al.* Corticothalamic feedback sculpts visual spatial integration in mouse thalamus. *Nat. Neurosci.* 1–10 (2021) doi:10.1038/s41593-021-00943-0.
2. Wang, Q., Webber, R. M. & Stanley, G. B. Thalamic synchrony and the adaptive gating of information flow to cortex. *Nat. Neurosci.* **13**, 1534–1541 (2010).
3. Mukherjee, A., Lam, N. H., Wimmer, R. D. & Halassa, M. M. Thalamic circuits for independent control of prefrontal signal and noise. *Nature* (2021) doi:10.1038/s41586-021-04056-3.
4. Aru, J., Suzuki, M. & Larkum, M. E. Cellular Mechanisms of Conscious Processing. *Trends Cogn. Sci.* **24**, 814–825 (2020).
5. Shepherd, G. M. G. & Yamawaki, N. Untangling the cortico-thalamo-cortical loop: cellular pieces of a knotty circuit puzzle. *Nat. Rev. Neurosci.* (2021) doi:10.1038/s41583-021-00459-3.
6. Guo, K., Yamawaki, N., Barrett, J. M., Tapies, M. & Shepherd, G. M. G. Cortico-Thalamo-Cortical Circuits of Mouse Forelimb S1 Are Organized Primarily as Recurrent Loops. *J. Neurosci.* **40**, 2849–2858 (2020).
7. Olsen, S. R., Bortone, D. S., Adesnik, H. & Scanziani, M. Gain control by layer six in cortical circuits of vision. *Nature* **483**, 47–52 (2012).
8. Bortone, D. S., Olsen, S. R. & Scanziani, M. Translaminar Inhibitory Cells Recruited by Layer 6 Corticothalamic Neurons Suppress Visual Cortex. *Neuron* **82**, 474–485 (2014).
9. Frandolig, J. E. *et al.* The Synaptic Organization of Layer 6 Circuits Reveals Inhibition

as a Major Output of a Neocortical Sublamina. *Cell Rep.* **28**, 3131-3143.e5 (2019).

10. Mease, R. a., Krieger, P. & Groh, A. Cortical control of adaptation and sensory relay mode in the thalamus. *Proc. Natl. Acad. Sci. U. S. A.* **111**, 6798–6803 (2014).
11. Hasse, J. M. & Briggs, F. Corticogeniculate feedback sharpens the temporal precision and spatial resolution of visual signals in the ferret. *Proceedings of the National Academy of Sciences* **114**, E6222–E6230 (2017).
12. Spacek, M. A. *et al.* Robust effects of corticothalamic feedback and behavioral state on movie responses in mouse dLGN. *Elife* **11**, (2022).
13. Guo, W., Clause, A. R., Barth-Maron, A. & Polley, D. B. A Corticothalamic Circuit for Dynamic Switching between Feature Detection and Discrimination. *Neuron* **95**, 180-194.e5 (2017).
14. Crandall, S. R., Cruikshank, S. J. & Connors, B. W. A corticothalamic switch: controlling the thalamus with dynamic synapses. *Neuron* **86**, 768–782 (2015).
15. Kuner, R. & Kuner, T. Cellular Circuits in the Brain and Their Modulation in Acute and Chronic Pain. *Physiol. Rev.* **101**, 213–258 (2021).
16. Prescott, S. a., Ma, Q. & De Koninck, Y. Normal and abnormal coding of somatosensory stimuli causing pain. *Nat. Neurosci.* **17**, 183–191 (2014).
17. Baliki, M. N. & Apkarian, A. V. Nociception, Pain, Negative Moods, and Behavior Selection. *Neuron* **87**, 474–491 (2015).
18. Vierck, C. J., Whitsel, B. L., Favorov, O. V., Brown, A. W. & Tommerdahl, M. Role of primary somatosensory cortex in the coding of pain. *Pain* **154**, 334–344 (2013).
19. Patel, R. & Dickenson, A. H. Neuronal hyperexcitability in the ventral posterior thalamus of neuropathic rats: modality selective effects of pregabalin. *J. Neurophysiol.* **116**, 159–170 (2016).
20. Iwata, M. *et al.* High-frequency stimulation in the ventral posterolateral thalamus reverses electrophysiologic changes and hyperalgesia in a rat model of peripheral

neuropathic pain. *Pain* **152**, 2505–2513 (2011).

21. LeBlanc, B. W. *et al.* Thalamic Bursts Down-regulate Cortical Theta and Nociceptive Behavior. *Sci. Rep.* **7**, 2482 (2017).
22. Song, Y. *et al.* Feedforward and feedback pathways of nociceptive and tactile processing in human somatosensory system: A study of dynamic causal modeling of fMRI data. *Neuroimage* **234**, 117957 (2021).
23. Lenz, F. A., Kwan, H. C., Dostrovsky, J. O. & Tasker, R. R. Characteristics of the bursting pattern of action potentials that occurs in the thalamus of patients with central pain. *Brain Res.* **496**, 357–360 (1989).
24. Gerke, M. B., Duggan, A. W., Xu, L. & Siddall, P. J. Thalamic neuronal activity in rats with mechanical allodynia following contusive spinal cord injury. *Neuroscience* **117**, 715–722 (2003).
25. Hains, B. C., Saab, C. Y. & Waxman, S. G. Changes in electrophysiological properties and sodium channel Nav1.3 expression in thalamic neurons after spinal cord injury. *Brain* **128**, 2359–2371 (2005).
26. Xiong, W. *et al.* Enhancing excitatory activity of somatosensory cortex alleviates neuropathic pain through regulating homeostatic plasticity. *Sci. Rep.* **7**, 12743 (2017).
27. Monconduit, L., Lopez-Avila, A., Molat, J.-L., Chalus, M. & Villanueva, L. Corticofugal output from the primary somatosensory cortex selectively modulates innocuous and noxious inputs in the rat spinothalamic system. *J. Neurosci.* **26**, 8441–8450 (2006).
28. Gross, J., Schnitzler, A., Timmermann, L. & Ploner, M. Gamma oscillations in human primary somatosensory cortex reflect pain perception. *PLoS Biol.* **5**, e133 (2007).
29. Tan, L. L. *et al.* Gamma oscillations in somatosensory cortex recruit prefrontal and descending serotonergic pathways in aversion and nociception. *Nat. Commun.* **10**, 983 (2019).
30. Groh, A., Krieger, P., Mease, R. A. & Henderson, L. Acute and Chronic Pain Processing

in the Thalamocortical System of Humans and Animal Models. *Neuroscience* **387**, 58–71 (2018).

31. Tan, L. L. & Kuner, R. Neocortical circuits in pain and pain relief. *Nat. Rev. Neurosci.* **22**, 458–471 (2021).
32. Rainville, P., Duncan, G. H., Price, D. D., Carrier, B. & Bushnell, M. C. Pain affect encoded in human anterior cingulate but not somatosensory cortex. *Science* **277**, 968–971 (1997).
33. Bushnell, M. C. *et al.* Pain perception: is there a role for primary somatosensory cortex? *Proc. Natl. Acad. Sci. U. S. A.* **96**, 7705–7709 (1999).
34. Uhelski, M. L., Davis, M. A. & Fuchs, P. N. Pain affect in the absence of pain sensation: evidence of asomaesthesia after somatosensory cortex lesions in the rat. *Pain* **153**, 885–892 (2012).
35. Tan, L. L. *et al.* A pathway from midcingulate cortex to posterior insula gates nociceptive hypersensitivity. *Nat. Neurosci.* **20**, 1591–1601 (2017).
36. Fields, H. L. Pain and the primary somatosensory cortex. *Pain* vol. 153 742–743 (2012).
37. Canavero, S. & Bonicalzi, V. Role of primary somatosensory cortex in the coding of pain. *Pain* vol. 154 1156–1158 (2013).
38. Mease, R. A. & Gonzalez, A. J. Corticothalamic Pathways From Layer 5: Emerging Roles in Computation and Pathology. *Front. Neural Circuits* **15**, 88 (2021).
39. Cichon, J., Blanck, T. J. J., Gan, W.-B. & Yang, G. Activation of cortical somatostatin interneurons prevents the development of neuropathic pain. *Nat. Neurosci.* **20**, 1122–1132 (2017).
40. Liu, Y. *et al.* Touch and tactile neuropathic pain sensitivity are set by corticospinal projections. *Nature* **561**, 547–550 (2018).
41. Jung, S.-C. *et al.* Corticothalamic modulation on formalin-induced change of VPM thalamic activities. *Neuroreport* **15**, 1405–1408 (2004).

42. Kim, J., Matney, C. J., Blankenship, A., Hestrin, S. & Brown, S. P. Layer 6 Corticothalamic Neurons Activate a Cortical Output Layer, Layer 5a. *Journal of Neuroscience* **34**, 9656–9664 (2014).
43. Minett, M. S., Quick, K. & Wood, J. N. Behavioral Measures of Pain Thresholds. *Curr. Protoc. Mouse Biol.* **1**, 383–412 (2011).
44. Deuis, J. R., Dvorakova, L. S. & Vetter, I. Methods Used to Evaluate Pain Behaviors in Rodents. *Front. Mol. Neurosci.* **10**, 284 (2017).
45. Bradman, M. J. G., Ferrini, F., Salio, C. & Merighi, A. Practical mechanical threshold estimation in rodents using von Frey hairs/Semmes–Weinstein monofilaments: Towards a rational method. *J. Neurosci. Methods* **255**, 92–103 (2015).
46. Boada, M. D. & Woodbury, C. J. Myelinated skin sensory neurons project extensively throughout adult mouse substantia gelatinosa. *J. Neurosci.* **28**, 2006–2014 (2008).
47. Boada, M. D., Danilo Boada, M. & Jeffery Woodbury, C. Physiological Properties of Mouse Skin Sensory Neurons Recorded Intracellularly In Vivo: Temperature Effects on Somal Membrane Properties. *Journal of Neurophysiology* vol. 98 668–680 (2007).
48. Cheah, M., Fawcett, J. W. & Andrews, M. R. Assessment of Thermal Pain Sensation in Rats and Mice Using the Hargreaves Test. *Bio Protoc* **7**, (2017).
49. Wallstrom, G., Liebner, J. & Kass, R. E. An Implementation of Bayesian Adaptive Regression Splines (BARS) in C with S and R Wrappers. *J. Stat. Softw.* **26**, 1–21 (2008).
50. Kirchgessner, M. A., Franklin, A. D. & Callaway, E. M. Distinct “driving” versus “modulatory” influences of different visual corticothalamic pathways. *Curr. Biol.* **31**, 5121-5137.e7 (2021).
51. Bruno, R. M. & Sakmann, B. Cortex is driven by weak but synchronously active thalamocortical synapses. *Science* **312**, 1622–1627 (2006).
52. de Kock, C. P. J., Bruno, R. M., Spors, H. & Sakmann, B. Layer- and cell-type-specific

suprathreshold stimulus representation in rat primary somatosensory cortex. *J. Physiol.* **581**, 139–154 (2007).

53. Vélez-Fort, M. *et al.* The stimulus selectivity and connectivity of layer six principal cells reveals cortical microcircuits underlying visual processing. *Neuron* **83**, 1431–1443 (2014).
54. Pauzin, F. P. & Krieger, P. A Corticothalamic Circuit for Refining Tactile Encoding. *Cell Rep.* **23**, 1314–1325 (2018).
55. Vestergaard, M., Carta, M. & Poulet, J. F. A. The cellular coding of temperature in the mammalian cortex. *bioRxiv* 2022.02.21.481299 (2022) doi:10.1101/2022.02.21.481299.
56. Milenkovic, N. *et al.* A somatosensory circuit for cooling perception in mice. *Nat. Neurosci.* **17**, 1560–1566 (2014).
57. Groh, A., de Kock, C. P. J., Wimmer, V. C., Sakmann, B. & Kuner, T. Driver or coincidence detector: modal switch of a corticothalamic giant synapse controlled by spontaneous activity and short-term depression. *J. Neurosci.* **28**, 9652–9663 (2008).
58. Alhadeff, A. L. *et al.* A Neural Circuit for the Suppression of Pain by a Competing Need State. *Cell* **173**, 140-152.e15 (2018).
59. Zhou, W. *et al.* Sound induces analgesia through corticothalamic circuits. *Science* **377**, 198–204 (2022).
60. Sillito, A. M., Jones, H. E., Gerstein, G. L. & West, D. C. Feature-linked synchronization of thalamic relay cell firing induced by feedback from the visual cortex. *Nature* **369**, 479–482 (1994).
61. Kirchgessner, M. A., Franklin, A. D. & Callaway, E. M. Context-dependent and dynamic functional influence of corticothalamic pathways to first- and higher-order visual thalamus. *Proc. Natl. Acad. Sci. U. S. A.* **117**, 13066–13077 (2020).
62. Gehrlach, D. A. *et al.* A whole-brain connectivity map of mouse insular cortex. *Elife* **9**, (2020).

63. Odoj, K. *et al.* In vivo mechanisms of cortical network dysfunction induced by systemic inflammation. *Brain Behav. Immun.* (2021) doi:10.1016/j.bbi.2021.05.021.

64. Kasanetz, F. & Nevian, T. Increased burst coding in deep layers of the ventral anterior cingulate cortex during neuropathic pain. *Sci. Rep.* **11**, 24240 (2021).

65. Moreno-Lopez, Y., Bichara, C., Delbecq, G., Isope, P. & Cordero-Erausquin, M. The corticospinal tract primarily modulates sensory inputs in the mouse lumbar cord. *Elife* **10**, (2021).

66. Masri, R. *et al.* Zona incerta: a role in central pain. *J. Neurophysiol.* **102**, 181–191 (2009).

67. Park, A., Uddin, O., Li, Y., Masri, R. & Keller, A. Pain After Spinal Cord Injury Is Associated With Abnormal Presynaptic Inhibition in the Posterior Nucleus of the Thalamus. *J. Pain* **19**, 727.e1-727.e15 (2018).

68. Ploner, M., Sorg, C. & Gross, J. Brain Rhythms of Pain. *Trends Cogn. Sci.* **xx**, 1–11 (2016).

69. Moseley, G. L. & Flor, H. Targeting cortical representations in the treatment of chronic pain: a review. *Neurorehabil. Neural Repair* **26**, 646–652 (2012).

70. Deisseroth, K. Predicted irradiance values: model based on direct measurements in mammalian brain tissue. (2012).

71. Stringer, C. *et al.* Spontaneous behaviors drive multidimensional, brain-wide activity. doi:10.1101/306019.

72. Montijn, J. S. *et al.* A parameter-free statistical test for neuronal responsiveness. *Elife* **10**, (2021).

73. Onodera, K. & Kato, H. K. Translaminar recurrence from layer 5 suppresses superficial cortical layers. *Nat. Commun.* **13**, 1–16 (2022).